



HAL
open science

New gas radiation model of high accuracy based on the principle of weighted sum of gray gases

Fatmir Asllanaj, Sylvain Contassot-Vivier, Guilherme C Fraga, Francis H.R. França, Roberta J.C. da Fonseca

► **To cite this version:**

Fatmir Asllanaj, Sylvain Contassot-Vivier, Guilherme C Fraga, Francis H.R. França, Roberta J.C. da Fonseca. New gas radiation model of high accuracy based on the principle of weighted sum of gray gases. *Journal of Quantitative Spectroscopy and Radiative Transfer*, 2024, 315, pp.108887. 10.1016/j.jqsrt.2023.108887 . hal-04375649

HAL Id: hal-04375649

<https://hal.science/hal-04375649>

Submitted on 5 Jan 2024

HAL is a multi-disciplinary open access archive for the deposit and dissemination of scientific research documents, whether they are published or not. The documents may come from teaching and research institutions in France or abroad, or from public or private research centers.

L'archive ouverte pluridisciplinaire **HAL**, est destinée au dépôt et à la diffusion de documents scientifiques de niveau recherche, publiés ou non, émanant des établissements d'enseignement et de recherche français ou étrangers, des laboratoires publics ou privés.



Distributed under a Creative Commons Attribution - NonCommercial - NoDerivatives 4.0 International License

New gas radiation model of high accuracy based on the principle of weighted sum of gray gases

Fatmir Asllanaj^{1*}, Sylvain Contassot-Vivier², Guilherme C. Fraga³, Francis H. R.

França³, Roberta J. C. da Fonseca³

¹ Université de Lorraine, CNRS, LEMTA, F-54000 Nancy, France

² Université de Lorraine, LORIA, UMR 7503, Vandoeuvre-lès-Nancy, F-54500, France

³ Universidade Federal do Rio Grande do Sul, Department of Mechanical Engineering,

Porto Alegre, RS 90050-170, Brazil

* Correspondence author - Phone : (33) (0)3 72 74 42 73

E-mail: Fatmir.Asllanaj@univ-lorraine.fr

Abstract The standard WSGG (Weighted Sum of Gray Gases) model is very fast and simple but can lead to relatively high discrepancies in the computation of the radiative heat transfer. A new model of high accuracy relying on the principle of the WSGG model is proposed. Contrary to the standard WSGG model, the pressure absorption coefficient depends here weakly on the temperature while the weighting factor is not predefined by a mathematical function. Mathematical properties on the model parameters are obtained and we show that all the model parameters can be determined from only one of them. This last is reconstructed with an efficient inverse algorithm from the total radiative heat source data computed with the LBL method using HITEMP 2010. We propose an efficient method to find good initial guesses (of the model parameters) leading to the best accuracy of the model. It is shown, on 17 selected 1D cases representative of the combustion of CO₂-H₂O mixtures, that the maximum relative errors on the radiative heat source for the new model (based on 6 gray gases) does not exceed 3.5% (for these 17 cases) whereas for the standard WSGG model, these errors vary up to 14.5% (five cases have errors higher than 10.0% and nine cases have errors between 5.0% and 10.0%). The accuracy of the total radiative heat flux is also greatly enhanced with the new model. We also show that the present model is robust and can be used in 3D geometry.

1 Introduction

Simulation of thermal radiative heat transfer in non-gray participating media is of interest to a wide range of fields, from atmospheric and weather-related processes [1] to combustion systems and other high-temperature applications [2,3]. For participating species such as H₂O and CO₂, the absorption coefficient κ_η has strong, erratic variations across the radiation wavenumber η , and its accurate representation requires either very expensive calculations or the careful selection of an appropriate spectral model [4]. Currently, the models regarded to provide the best compromise between cost and accuracy for engineering calculations fall within the class of global models [5], of which one of the most widely used is the Weighted-Sum-of-Gray-Gases (WSGG) model [6–8].

The WSGG model represents the κ_η spectrum as a small number of gray gases that occupy non-contiguous regions across the spectrum. The Radiative Transfer Equation (RTE) may then be written and solved for each gray gas separately; the total radiative intensity is given as a summation over the radiative intensities of each gas. Despite such a simple formulation, previous works have shown that the WSGG model is able to predict the radiative heat source S_r and radiative heat flux Q_r with error as high as about 15 to 20% across many different conditions (see, for instance, the brief review of the model presented by Fraga et al. [9]). More recent and advanced global models exist, such as the Spectral Line WSGG (SLW) [10, 11] and the Full-Spectrum k -distribution (FSK) [12] models.

Typically, each gray gas k in the WSGG model has two properties associated to it: an absorption coefficient, κ_k , and an emission-weight factor, w_k . Both quantities are related to the local thermodynamic state using simple expressions, which in the WSGG literature are referred to as “correlations.” The first correlations were given between the 1960s and 1980s, but especially the last decade has seen a surge in new correlations. Those are based on up-to-date, high-resolution spectral databases (usually, HITEMP 2010 [13]), and are designed for specific scenarios, for example, air-fuel combustion (e.g., [14–16]); oxy-fuel combustion [17–19]; radiation from soot, coal and other particulate media [20, 21]; and high-pressure conditions [22–26].

With but a few exceptions, those previous WSGG correlations were determined by fitting total emissivity across a sufficiently wide range of thermodynamic conditions and path lengths. Although the exact procedure varies depending on the work, this generally involves multiple linear or multivariate regressions; the final values of the constants that make up the correlations are somewhat dependent on the initial guesses. Detailed descriptions of different fitting procedures are given in Refs. [15, 17, 19], for example.

The choice of total emissivity fittings as the basis for constructing the WSGG correlations is due to both historical and practical reasons. The first applications of the WSGG model were done in the framework of the zonal method, where

the model served as a convenient way to compute emissivities. Also, emissivity charts determined experimentally were available at the time, and those could be used as the reference for the determining the correlations. Since then, emissivity charts were replaced by datasets of emissivity computed by a wide-band model or by line-by-line (LBL) method of high-resolution absorption spectra, and the WSGG model was shown to be applicable to any RTE solution method; however, the general method for producing the correlations for the model was retained.

A notable exception is the series of works by Guo et al. [27–29], where expressions for κ_k and w_k were determined by fitting these quantities to their counterparts in the FSK model for a four-point Gauss quadrature scheme. Following this procedure, WSGG correlations were constructed for atmospheric [27] and high-pressure [29] mixtures of CO₂ and H₂O, and for ash particles [28]. All fittings were carried out across a wide range of temperatures and (when applicable) CO₂-H₂O mole fraction ratios, but changes in path length were not considered. In addition, adequate predictions of Q_r and S_r (comparable to those of other recent WSGG models) were reported for a sample of 1D test cases involving non-uniform scalar profiles.

More recently, another method for obtaining the WSGG correlations was introduced by Asllanaj et al. [30]. The parameters of the model were determined using an inverse algorithm and the adjoint state of the RTE, with the cost function defined based on the local total radiative heat source. An important feature of such approach is that, if applied to a single case, the resulting WSGG correlations have LBL-level accuracy even with only four gray gases. By averaging the spatially-varying correlations, a compact model was then produced, and extensive testing for one- and three-dimensional problems showed that its accuracy is generally at least on par (but usually better) than standard WSGG correlations [30]. It should be noted that, while the formulations of Guo et al. [27–29] and Asllanaj et al. [30] share some of the characteristics of the standard WSGG model, they were not derived from the assumptions of the WSGG model. For the model of Refs. [27–29], one may argue that it has some relationship to the WSGG model since the correlations were obtained from the FSK method, which in turn is related to that model [31]. Conversely, there is no connection of the inverse algorithm-based correlations of Ref. [30] to the standard WSGG model, except from the fact that the total intensity is still given as a sum of intensities determined by solving consecutive, independent RTEs, and that to each of these RTEs there is an associated absorption coefficient κ_k and emission-weight coefficient w_k . Therefore, while the approach introduced in [30] is a WSGG model, it still differs considerably of the WSGG models broadly studied in the literature.

The objective of this work is to develop a new gas radiation model of high accuracy starting from [30]. The model proposed in [30] had two limitations. First, it was not possible to use the parameters that are spatially dependent (determined for a given test case) on other test cases in forward calculation. Second, the gray gas absorption coefficients $\kappa_{p,k}$ were path-

length dependent. This is no longer the case for the new model proposed in this work. In order to have a model of high accuracy, we show in the present paper that $\kappa_{p,k}$ need to depend weakly on the temperature. We also show that it is better to not predefine the weighting factors w_k by a mathematical expression (they were linear functions of the temperature in [30]), but rather to let the inverse algorithm to seek their profiles. In this way, we obtain mathematical properties on the model parameters and we show that all the model parameters can be determined from only one of them. This last is reconstructed using an inverse algorithm with the S_r data (computed with the LBL method using HITEMP 2010). We show that the parameters (determined for a given test case) are functions of temperature and thus can be applied to other test cases. Finally, we develop an efficient algorithm that finds good initial guesses (of the model parameters) to optimize the model accuracy. In the present work, a new optimization procedure to determine the model parameters is thus proposed and the model accuracy is greatly improved compared to the one of [30].

The paper has three main sections. The next section concerns the theoretical analyses of the forward and inverse problems. The inverse problem consists in reconstructing the model parameters. Section 3 then presents results obtained with the inverse and new forward models. Radiative heat transfer (RHT) test cases are studied in Section 4, considering non-isothermal and inhomogeneous participating gases. The accuracy and performance of the new model are studied and the results are assessed using LBL and WSGG solutions of the literature. The last section deals with conclusions and future perspectives.

2 Theoretical analyses

2.1 Forward model

A non-gray absorbing and emitting medium is considered in this work. In its multidimensional formulation, the spectral RTE is given by [5]:

$$\boldsymbol{\Omega} \cdot \nabla I_\eta(s, \boldsymbol{\Omega}) = \kappa_\eta(s) \left\{ I_{b,\eta}[T(s)] - I_\eta(s, \boldsymbol{\Omega}) \right\}, \quad (1)$$

where η is the wavenumber, $\boldsymbol{\Omega}$ is the direction of propagation of radiation, T is the medium temperature and $I_\eta(s, \boldsymbol{\Omega})$ is the spectral radiative intensity in the $\boldsymbol{\Omega}$ direction along the path length s . The spectral absorption coefficient of the medium is denoted κ_η and $I_{b,\eta}[T]$ is the spectral Planck function at temperature T .

In the 1D formulation of the non-gray WSGG model, the RTE can be established for the k -th gray gas, in the μ direction along the path x , as: [5, 15, 30, 32–34]:

$$\mu \frac{\partial I_k^+(x, \mu)}{\partial x} + \kappa_{p,k}(x) p_a(x) \left\{ I_k^+(x, \mu) - w_k(x) I_b[T(x)] \right\} = 0, \quad (2)$$

$$-\mu \frac{\partial I_k^-(x, -\mu)}{\partial x} + \kappa_{p,k}(x) p_a(x) \left\{ I_k^-(x, -\mu) - w_k(x) I_b[T(x)] \right\} = 0, \quad (3)$$

for $x \in \mathcal{D} = [0, L]$ (where L is medium length) and $\mu \in \Sigma^+ = \{\mu, 0 < \mu \leq 1\}$. The index k varies between 0 and K where K denotes the number of gray gases. The coefficient $\kappa_{p,k}$ is the pressure absorption coefficient of the k -th gray gas. While this coefficient is assumed to be constant in the standard WSGG model, in the present study it depends on the position x through the temperature T (as will be seen later). The coefficient p_a is the sum of the partial pressures of the species that form the mixture. The Planck function at temperature T is formulated as:

$$I_b[T] = \frac{\sigma T^4}{\pi}, \quad (4)$$

where σ is the Stefan-Boltzmann constant. Here, $I_k^+(x, \mu)$ is the partial radiative intensity of gas k at the spatial position x , in the forward direction; $I_k^-(x, \mu)$ is the partial radiative intensity of gas k at the spatial position x , in the backward direction. Then, the partial radiative intensity of gas k at the position x , in all direction $\mu \in \Sigma = \{\mu \neq 0, -1 \leq \mu \leq 1\}$, is given by:

$$I_k(x, \mu) = \left\{ \begin{array}{ll} I_k^+(x, \mu) & \mu \in \Sigma^+ \\ I_k^-(x, -\mu) & \mu \in \Sigma^- \end{array} \right\},$$

where the index k varies between 0 and K . The coefficient w_k is the weighting factor. In the standard WSGG model [15, 33], as well as in the model presented in our previous work [30], w_k is written with polynomial functions of the temperature T , as below:

$$w_k[T] = \sum_{l=0}^K b_{k,l} T^l, \quad (5)$$

in which $b_{k,l}$ are constant polynomial coefficients. In this work, w_k is not predefined by a mathematical function; rather, just as $\kappa_{p,k}$, it only depends on the position x through the temperature T (as will be seen later).

Originally, the WSGG model was introduced by Hottel [6] to compute the total gas emissivity of a layer (of thickness L), of a gas mixture at temperature T . Hottel and Sarofim [7] gave two interpretations describing the physical meaning of the two coefficients $\kappa_{p,k}$ and w_k . The first interpretation is a physical one and considers that w_k represents the fraction of blackbody emission in the sections of the spectrum where the spectral pressure absorption coefficient is $\kappa_{p,k}$. The second interpretation considers $\kappa_{p,k}$ and w_k as simple parameters allowing a precise adjustment on the total gas emissivity data. In the present study, the RTE given by Eqs. (2) and (3) is considered as a fitting model, i.e. a homogenized model with effective parameters $\kappa_{p,k}$ and w_k ; therefore, the second interpretation of Hottel and Sarofim is adopted, except that the precise adjustment is made on the total radiative heat source data (computed with the LBL method) instead of the total gas emissivity data [30].

The weighting factors w_k are computed only for the gray gases. To take into account the transparent windows, the corresponding weighting factor and the pressure absorption coefficient are computed with the subscript k set equal to zero ($\kappa_{p,k=0} = 0$), as in the standard WSGG model. For an infinitely thick gas, the total emissivity tends to unity. Then, it follows:

$$w_0 = 1 - \sum_{k=1}^K w_k. \quad (6)$$

The present study is applied to black walls. Then, Eqs. (2) and (3) are subjected to the following boundary conditions [5, 15, 32]:

$$I_k^+(x=0, \mu) - w_k(x=0) I_b[T(x=0)] = 0, \quad (7)$$

$$I_k^-(x=L, -\mu) - w_k(x=L) I_b[T(x=L)] = 0, \quad (8)$$

for $\mu \in \Sigma^+$. The function $I_b[T]$ is the Planck function at the wall temperature. Once the partial radiative intensity I_k has been computed for all K gray gases in the model, the summation required for evaluating the total radiative intensity I , S_r and Q_r leads to:

$$I = \sum_{k=0}^K I_k, \quad (9)$$

$$Q_r(x) = 2\pi \sum_{k=0}^K \int_{-1}^1 I_k(x, \mu) \mu d\mu \quad \text{and} \quad S_r(x) = -\frac{dQ_r(x)}{dx} = G_\kappa(x) - 4\pi \kappa_P(x) I_b[T(x)], \quad (10)$$

with

$$G_\kappa(x) = 2\pi p_a(x) \sum_{k=1}^K \kappa_{p,k}(x) \int_{-1}^1 I_k(x, \mu) d\mu \quad \text{and} \quad \kappa_P(x) = p_a(x) \sum_{k=1}^K \kappa_{p,k}(x) w_k(x), \quad (11)$$

where κ_P denotes the Planck-mean absorption coefficient.

2.2 Formulation of the inverse problem

2.2.1 Cost function

Let J be a cost function which is an explicit function of the model parameters. In this work, the function J represents the relative discrepancy between the total radiative heat source computed with the LBL method, $S_{r,\text{LBL}}$ and the one obtained with the present model, $S_r(\theta)$:

$$J(\theta) = \frac{1}{2} \left\| \frac{S_r(\theta) - S_{r,\text{LBL}}}{(S_{r,\text{LBL}})_{\max}} \right\|^2, \quad (12)$$

in which θ represents one of parameters $(\kappa_{p,k}, w_k)_{1 \leq k \leq K}$ and $(S_{r,\text{LBL}})_{\max}$ is the absolute value of the maximum of $S_{r,\text{LBL}}$. The norm in Eq. (12) is associated to the inner product of square-integrable real-valued functions of the Hilbert space. Eq. (12) is a new constraint in the model which should allow to compute $S_r(\theta)$ with a better accuracy. The

aim in this work is to reconstruct the parameters of interest $\kappa_{p,k}$ and w_k for the present model. Then, the parameters vector $\theta = (\kappa_{p,k}, w_k)_{1 \leq k \leq K}$ can be reconstructed by applying a Gradient-Based Optimization Algorithm (GBOA) to the function J .

2.2.2 Inverse algorithm

The GBOA using the quasi-Newton method with Lm-BFGS [35] was used to minimize, in an iterative procedure, the cost function J given by Eq. (12). Let d be a search direction of gradient used in gradient descent. Then, the GBOA iteratively updates the parameters vector θ along d as:

$$\theta^{(n+1)} = \theta^{(n)} + \alpha^{(n)} d (\nabla J(\theta^{(n)})), \quad (13)$$

where n is the iteration number and $\alpha^{(n)}$ is the step size given by the Armijo backtracking line search [36]. The update steps have to be small enough for the convergence of the algorithm. Thus, by lowering the value of α^n in the update of Eq. (13), some tests were carried out following the principle of under-relaxation factors. The cost function's gradient over the parameter θ denoted $\nabla J(\theta)$ is needed in Eq. (13). Simplified expressions of the gradients over the parameter $\kappa_{p,k}$ and w_k were used in the inverse algorithm. From Eq. (66) of Appendix A, they are given by:

$$\nabla J(w_k)(x) = -\frac{(S_r(x) - S_{r,\text{LBL}}(x))}{(S_{r,\text{LBL}})_{\text{max}}^2} \quad \text{and} \quad \nabla J(\kappa_{p,k}) = -\nabla J(w_k). \quad (14)$$

The calculations of the cost function's gradients and the justification of expressions (14) are detailed in Appendix A. It is worth noting that the gradients do not depend on the index k . This leads to the model parameters $\kappa_{p,k}$ and w_k are computed similarly for each index k . Thus, they depend mainly on their initial guesses as shown in Appendix C. Also, It is worth noting that the right hand side of Eq. (14) is not gradient because it is a simplified (approximated) expression for the cost function's gradients over w_k .

2.2.3 Scaling procedure

A scaling procedure needs to be used for the reconstruction of the model parameters [30]. Then, the cost function's gradients over $\kappa_{p,k}$ and w_k given by Eqs. (14) can be scaled as:

$$\nabla J^{\text{scaled}}(w_k) = c_{w_k} \nabla J(w_k) \quad \text{and} \quad \nabla J^{\text{scaled}}(\kappa_{p,k}) = c_{\kappa_{p,k}} \nabla J(\kappa_{p,k}), \quad (15)$$

in which c_{w_k} and $c_{\kappa_{p,k}}$ are scaling coefficients. They can be computed after the first iteration of the inverse process as:

$$c_{w_k} = \frac{d_{w_k}}{\max(|\nabla J(w_k^{(0)})|)} \quad \text{and} \quad c_{\kappa_{p,k}} = \frac{d_{\kappa_{p,k}}}{\max(|\nabla J(\kappa_{p,k}^{(0)})|)}, \quad (16)$$

and the same values were used during the iterations. To have the same profiles for w_k , d_{w_k} need to have the same values for all the indices k . In the same way, to have the same profiles for $\kappa_{p,k}$, $d_{\kappa_{p,k}}$ need to have the same values for all the indices k . The best estimation of the parameters were found when:

$$d_{w_k}(x) = p_a(x) \quad \text{and} \quad d_{\kappa_{p,k}} = \frac{1}{L}, \quad (17)$$

where $p_a(x)$ is the sum of the partial pressures of the species and L is the domain length. The choice of these scalings is justified to have a dimensionally consistent relation on the model parameters as presented in Appendix C.

2.2.4 Mathematical properties on the model parameters

As it will be presented in Section 3.2, the model parameters will be reconstructed for a reference state (reference test case) with a constant reference coefficient p_a^{ref} and only the reference temperature changes for this test case. Each spatial position x corresponds to one value of the temperature T ; then, the coefficients $\kappa_{p,k}$ and w_k are, in fact, functions of the temperature. Mathematical relations on the model parameters were obtained (see Appendix C) and are summarized below. From the previous remark, these relations can be expressed as functions of temperature T :

$$\kappa_{p,k}[T] = \kappa_{p,1}[T] + \left(\kappa_{p,k}^{(0)} - \kappa_{p,1}^{(0)} \right) \quad \forall 2 \leq k \leq K, \quad (18)$$

$$w_k[T] = w_1[T] + \left(w_k^{(0)} - w_1^{(0)} \right) \quad \forall 2 \leq k \leq K, \quad (19)$$

$$L^{\text{ref}} p_a^{\text{ref}} \kappa_{p,1}[T] + w_1[T] = L^{\text{ref}} p_a^{\text{ref}} \kappa_{p,1}^{(0)} + w_1^{(0)}, \quad (20)$$

where L^{ref} is the reference length. Here, the coefficients $\kappa_{p,k}^{(0)}$ and $w_k^{(0)}$ are the constant initial guesses of $\kappa_{p,k}$ and w_k , respectively, for the case solved by inverse method. The effective parameters of the homogenized model mentioned at the beginning are $\kappa_{p,k}$ and w_k . It is remarkable to see that all the parameters $\kappa_{p,k}$ and w_k can be determined from only one of them, for instance w_1 , and $\kappa_{p,1}$ is deduced from Eq. (20). Then, in this work, only w_1 was reconstructed by inverse method. Nevertheless, we checked that the same values of model parameters are obtained if they are all reconstructed by inverse method.

3 Results

The model was used to solve RHT in inhomogeneous and non-isothermal participating gases. The 1D test cases presented in this section were selected, in one hand, to calibrate the present model and, on the other hand, to evaluate its accuracy. Especially for the first point, it was necessary to select well-known test cases from the literature representative of the

combustion of CO₂-H₂O mixtures where the standard WSGG model lead to higher errors [15, 30, 37]. As in the test cases presented in these references, the upper bound of the temperature range are limited to 1,800 K, the same upper bound of the temperature range has been used in the present work.

The coefficient p_a is defined as: $p_a(x) = [Y_{\text{CO}_2}(x) + Y_{\text{H}_2\text{O}}(x)] p$ where Y is the mole fraction and p is the total pressure. The CO₂-H₂O mixture has a fixed mole ratio of $Y_{\text{H}_2\text{O}}/Y_{\text{CO}_2} = 2$ for all the cases (including the 3D test case studied in section 3.5), and it is subjected to atmospheric pressure ($p = 1$ atm for all the cases). The temperature profile and the composition of the medium vary according to the test cases presented in the next.

Except for the search of the initial guesses of the model parameters, all the simulations were carried out with a 48 cores computer (12 cores/CPU, 2 CPUs Intel Xeon@2.4-3.5GHz) using Intel C compiler and Hyper-Threading.

To evaluate the model accuracy, the discrepancies between the solution of the present model and the one of the LBL method (for the results of S_r and Q_r) are computed as maximum and average normalized errors:

$$\delta\varphi(x) = \frac{|\varphi(x) - \varphi_{\text{LBL}}(x)|}{\max(|\varphi_{\text{LBL}}|)} \cdot 100\%, \quad (21)$$

where the denominator of the fraction in Eq. (21) is the maximum absolute value of φ . Here, φ is either S_r and Q_r . In the next, the subscripts "avg" and "max" are used to indicate the average and maximum errors, respectively.

3.1 1D test cases studied

The proposed method has been applied to a 1D medium having by black walls, separated by a distance L . The model accuracy was evaluated by comparing its results with those of the LBL method and the standard WSGG model with the parameters by Dorigon et al. [15] based on HITEMP 2010. For the LBL solution, the absorption spectra was generated for temperatures ranging from 400 K to 1,800 K using a constant step of 100 K, and for the following values for $p_a = 0.01, 0.1, 0.2, 0.4, 0.6$ (at atmospheric pressure). The intermediary partial pressures and temperatures were evaluated using linear interpolations. It was shown in independent studies that the accuracy of LBL method was enough to evaluate the present model. The RTE has been solved both for the present model and LBL method with a mesh composed of 200 points using a constant step along the path. Thirty discrete directions were used for the angular discretization of the RTE. These spatial and angular discretizations led to insensitive results with the mesh according to [15].

3.1.1 Description of the test cases

Let $\hat{x} = x/L \in [0, 1]$ be the dimensionless distance from the left wall. Two symmetric and one asymmetric profiles (according to the x -axis) for the temperature and CO₂ mole fraction were considered:

$$T(\hat{x}) = 400 \text{ K} + (1,400 \text{ K}) \sin^2(\pi \hat{x}), \quad (22)$$

$$T(\hat{x}) = 400 \text{ K} + (1,400 \text{ K}) \sin^2(2\pi \hat{x}), \quad (23)$$

$$T(\hat{x}) = \begin{cases} 880 \text{ K} + (920 \text{ K}) \sin^2(2\pi \hat{x}) & \text{if } \hat{x} \leq 0.25 \\ 400 \text{ K} + (1,400 \text{ K}) \left(1 - \sin^{3/2}\left(\frac{2\pi}{3}(\hat{x} - 0.25)\right)\right) & \text{if } \hat{x} > 0.25 \end{cases} \quad (24)$$

$$Y_{\text{CO}_2}(\hat{x}) = 0.2 \sin^2(\pi \hat{x}), \quad (25)$$

$$Y_{\text{CO}_2}(\hat{x}) = 0.2 \sin^2(2\pi \hat{x}), \quad (26)$$

$$Y_{\text{CO}_2}(\hat{x}) = \begin{cases} 0.25 \sin^2(2\pi \hat{x}) & \text{if } \hat{x} \leq 0.25 \\ 0.25 \left(1 - \sin\left(\frac{2\pi}{3}(\hat{x} - 0.25)\right)\right) & \text{if } \hat{x} > 0.25 \end{cases} \quad (27)$$

For these first cases, the average mole fraction of CO₂ is equal to 0.1. All the cases studied in this work are listed in Table 1. The first twelve cases are taken from Dorigon et al. [15]. Additional test cases were selected to calibrate the proposed model and to further investigate its accuracy. Sinusoidal profiles for the temperature and species concentration were also considered:

$$T(\hat{x}) = 700 \text{ K} - (300 \text{ K}) \cos(\pi \hat{x}), \quad (28)$$

$$Y_{\text{CO}_2}(\hat{x}) = 0.1 - 0.075 \cos(\pi \hat{x}). \quad (29)$$

Two lengths $L = 1 \text{ m}$ and $L = 3 \text{ m}$ were considered for these profiles.

Hyperbolic profiles for the temperature and species concentration were also studied and are defined by:

$$T(\hat{x}) = 1,100 \text{ K} + (5,600 \text{ K}) \psi(\hat{x}) \quad \text{with} \quad \psi(\hat{x}) = (0.5 - \hat{x})^3, \quad (30)$$

$$Y_{\text{CO}_2}(\hat{x}) = 0.1 + 0.8 \psi(\hat{x}). \quad (31)$$

The three lengths $L = 0.25 \text{ m}$, $L = 1 \text{ m}$ and $L = 2 \text{ m}$ were considered for these profiles.

As before, the average mole fraction of CO₂, taken into account in these new cases, is equal to 0.1. The five new cases are reported in Table 1. Finally, the influence of the domain length L was also studied and the first case previously described was also considered for lengths L equal to 3, 4 and 5 m. These three new cases are the last three cases reported in Table 1.

[Table 1 about here.]

Figures 1(a) and 1(b) display the profiles of temperature and CO₂ mole fraction along the slab used in the test cases reported in Table 1.

[Figure 1 about here.]

3.1.2 Reference state for the reconstruction of the model parameters

A reference state is required in the model. Here, Case 1 was selected for the reconstruction of the model parameters because it is the simplest and the most representative (for the temperature and the mole fraction of CO₂) among all test cases. Different lengths L varying between 0.25 m and 5 m were studied (see Table 1). Case 1 considers the arbitrary length $L = 1$ m. The average mole fraction of CO₂, considered in all the cases, is equal to 0.1. Case 1 considers the arbitrary mole fraction of CO₂ equal to 0.1. The reference state required for the reconstruction of the model parameters presented in the next section is then the one of case 1:

$$L^{\text{ref}} = 1 \text{ m} ; Y_{\text{CO}_2}^{\text{ref}} = 0.1 ; Y_{\text{H}_2\text{O}}^{\text{ref}} = 0.2 ; p^{\text{ref}} = 1 \text{ atm}, \quad (32)$$

$$T^{\text{ref}}(\tilde{x}) = 400 \text{ K} + (1, 400 \text{ K}) \sin^2(\pi \tilde{x}) \quad \text{with} \quad \tilde{x} \in [0, 0.5], \quad (33)$$

The reference spatial mesh (of the interval $[0, 0.5]$) is composed to 100 points with a constant step (equal to 1/199 m). T^{ref} has then 100 discrete values evaluated on this reference spatial mesh.

3.2 Reconstruction of the model parameters

3.2.1 Step 1: Initial guesses

Arbitrary candidate values for the first initial guesses $\kappa_{p,k}^{(0)}$ and $w_k^{(0)}$ are required. We remarked that $\kappa_{p,1}^{(0)}$ can have a positive value between 0 and 1. In principle, it is sufficient to take only one high value for $\kappa_{p,k}^{(0)}$ (between 10 and 100). To optimize the calculations, a restricted domain for the first initial guesses can then be proposed as:

$$0 < \kappa_{p,1}^{(0)} \leq 1 \quad ; \quad 1 \leq \kappa_{p,k-1}^{(0)} \leq \kappa_{p,k}^{(0)} \leq 10 \quad \text{for} \quad k = 3, \dots, K-1 \quad ; \quad 10 \leq \kappa_{p,K}^{(0)} \leq 100, \quad (34)$$

$$0.1 < w_{k-1}^{(0)} \leq w_k^{(0)} \leq 0.5 \quad \text{for} \quad k = 2, \dots, K \quad \text{with} \quad 0 < \sum_{k=1}^K w_k^{(0)} \leq 1. \quad (35)$$

3.2.2 Step 2: Reconstruction by inverse method of the weighting factor w_1

The reconstruction by inverse method of the weighting factor w_1 for case 1, starting from the initial guess $w_1^{(0)}$, was carried out using the S_r data obtained with LBL calculations based on HITEMP 2010. The LBL calculations are detailed

in [15] and are not repeated here. The scaled cost function's gradient with respect to the weighting factor w_1 was computed according to Eqs. (15)-(17). With initial guess $w_1^{(0)}$, the weighting factor w_1 (reconstructed by inverse method) is obtained after about 4,000 iterations. Even if the iteration number is very high, the calculations are fast because they are 1D (about 3 s.). The typical convergence of the cost function $J(w_1)$ according to the iteration number is displayed in Fig. 2. The stopping criterion was related to a relative error of $J(w_1)$ which should be lower than a prescribed tolerance (set to 10^{-6}). At the beginning of the iterations, the convergence is very fast and then very slow.

[Figure 2 about here.]

3.2.3 Step 3: Procedure to reconstruct the other model parameters

The procedure to reconstruct all the model parameters for any arbitrary temperature T is deduced from the reference state Eq. (32) and Eqs. (18)-(20):

$$\kappa_{p,1}[T] = \frac{1}{0.3} \left(w_1^{(0)} - w_1[T] \right) + \kappa_{p,1}^{(0)}, \quad (36)$$

$$\kappa_{p,k}[T] = \kappa_{p,1}[T] + \left(\kappa_{p,k}^{(0)} - \kappa_{p,1}^{(0)} \right) \quad \forall 2 \leq k \leq K, \quad (37)$$

$$w_k[T] = w_1[T] + \left(w_k^{(0)} - w_1^{(0)} \right) \quad \forall 2 \leq k \leq K. \quad (38)$$

As it will be shown after, the model using 6 gray gases leads to the most accurate results. For this model, the values of the initial guesses are reported in Table 2.

[Table 2 about here.]

The weighting factor $w_1[T^{\text{ref}}]$ has 100 values on the reference spatial mesh. These values, reconstructed with the found initial guesses, for 6 gray gases, are reported in Table 3. For arbitrary T , $w_1[T]$ is obtained from $w_1[T^{\text{ref}}]$ through linear interpolation. It should be noticed that $T^{\text{ref}}(x)$ needs to be monotonic between 400 and 1,800 K. Using the Matlab polyfit function, we tried to represent $w_1[T]$ as a polynomial function of T . We realized that the procedure fitting needs to have a very high accuracy. In this case, it was better to use the linear interpolation procedure. To avoid linear interpolation problems using the lowest or the highest values of T (400 K and 1,800 K), these two temperatures values have been slightly modified by 399.99 K and 1,800.01 K, respectively. It should be noticed that the use of a reference spatial mesh composed of 500 points providing 500 values for the weighting factor $w_1[T^{\text{ref}}]$ does not improve significantly the model accuracy (less than 0.2%).

[Table 3 about here.]

3.2.4 Step 4: Cases solved in forward calculation

The model parameters obtained from the first three steps previously presented are used to solve in forward calculation Cases 2 to 17 of Table 1.

3.2.5 Overall algorithm

The problem to solve, defined by the steps 1 to 4 previously presented, is strongly non-linear and very sensitive to the initial guesses of the model parameters. These last should be chosen not far from the desired solution to ensure, in particular, the convergence of the inverse method of Step 2. This requires testing a large number of initial guesses of the model parameters. The inverse problem of Step 2 can have multiple accurate solutions and only one of them can be chosen. The objective is not only to find the most accurate solution for the steps 2 and 3 but also for Step 4. Thus, the model calibration is carried out with the steps 1 to 4. In this way, we can hope to find the best feasible solution for the cases 1 to 17 of Table 1, i.e., the one that is closest to the LBL reference solution. This does not imply that the solution found is dependent on the selected cases solved in forward calculation. These last are only used to help to find the best feasible solution for Cases 2 to 17. In fact, only some of these cases (the most complex ones) are really used to find the best feasible solution, which was found by the minimizations of the error function Γ in % defined as:

$$\Gamma = \max_{2 \leq \text{case} \leq 17} \delta S_{\max}. \quad (39)$$

The best feasible solution will be the one with the lowest normalized errors and uniformly distributed over all the cases. It is worth noting that Case 1 is included in the search of the initial guesses and that it is important to consider the same cases in the search of the initial guesses as those considered for model validation.

A manual "trial-and-error" procedure was first used to find good values of initial guesses. We proposed arbitrary candidate values and then solved the steps 2 and 3 and also step 4 to know if these candidate values were satisfactory. If this was not the case, we manually adjusted the values of initial guesses by adding small positive steps to each of them and then the steps 1 to 4 were repeated. This process continued until satisfactory values of initial guesses were obtained, which usually required some iterations. Furthermore, while the final solution may be acceptable, it was not optimal. Indeed, according to the continuous nature of the model parameters and the high variability of the results, a manual setting of the initial guesses (of the model parameters) is unsuitable. This is why we developed an efficient algorithm that can test a much larger sample of initial guesses, thus allowing to capture much better values (of initial guesses) and to obtain a better accuracy of the model.

So, we proposed to use an automatic parameters fitting according to the accuracy of the results compared to the those of the LBL method. The problem of parameters fitting is an optimization problem in which the parameters are the values to fit and the error function is the error of the proposed model according to the reference model. In our case, the criterion used to find the best feasible solution is to minimize the error function Γ (defined by (39)).

A common way to solve such problem is to use genetic algorithms (GA) [38]. They are inspired from the evolution theory and have proven to be efficient in numerous optimization problems. Genetic algorithms are iterative processes that start with an initial set of potential solutions and make them evolve at each iteration according to genetically inspired rules designed to make the set of solutions converge towards a local optimum in the search space. In our case, we have chosen a specific variant of GA that is called differential evolution, and that was introduced by [39] and used in parameters optimization of other complex simulations [40, 41]. The principle of differential evolution is to generate an initial set of potential solutions (vectors of parameters values), then at each iteration, new candidate solutions are generated by a geometric combination of three solutions at the previous iteration. Typically, the relation is of the form:

$$\mathbf{V}^j = \mathbf{W}_k^b + F \cdot (\mathbf{W}_k^l + \mathbf{W}_k^m), \quad (40)$$

where \mathbf{V}^j is the j^{th} intermediate solution at current iteration, \mathbf{W}_k^b is the best solution found at iteration k , $\mathbf{W}_k^{l,m}$ are randomly chosen solutions l and m at iteration k and F is a real in the interval $[0, 2]$. The value of F can be decreased during the genetic process when the error becomes small enough. This allows the process to focus on the final solution. Then, there is a probabilistic mixing step of parameters values (index i is the i^{th} element of the considered solution vector) from the intermediate solutions with some of the previous solutions, as follows:

$$\mathbf{Z}^j(i) = \begin{cases} \mathbf{V}^j(i) & \text{if } p = \mathcal{U}(0, 1) \text{ such that } p < C_R \in [0, 1] \\ \mathbf{W}_k^j(i) & \text{otherwise} \end{cases} \quad (41)$$

where $\mathcal{U}(0, 1)$ is the uniform distribution in $[0, 1]$ and C_R is a constant defined as the crossing rate. The final step is a selection of the solutions that are kept for the next iteration:

$$\mathbf{W}_{k+1}^j = \begin{cases} \mathbf{Z}^j & \text{if } \Gamma(\mathbf{Z}^j) \leq \Gamma(\mathbf{W}_k^j) \\ \mathbf{W}_k^j & \text{otherwise} \end{cases} \quad (42)$$

where Γ is the error that needs to be minimized.

Although this random iterative process does not theoretically ensure to find the optimal set of parameters, in practice, it converges towards a local optimum that allows us to correctly fit the model. However, it is quite long as it may require a lot of iterations in which computation steps 1 to 4 must be performed. So, we developed a parallel algorithm following

the master-workers model in order to distribute the evaluations of all candidate solutions over a set of machines. Hence, at each iteration, the different sets of parameters are dynamically distributed over the worker machines, each of them executing the calculation with one given set of parameters and comparing the results to the reference model in order to send back the error for this set to the master machine. All the genetic operations described above are performed on the master machine once all the evaluation results are received. Then, a new iteration is done until the stopping criteria is achieved.

One recurrent problem in GA lies in the stopping criteria because using a threshold over the error function Γ alone is generally not sufficient. Indeed, although the process is designed to converge towards an extremum of the error function Γ , there is no guarantee neither over its globality (it might be a local extremum) nor on the speed to reach it. So, a common practice is to check the evolution of the error function Γ between consecutive iterations as well as to add a maximal number of iterations or a maximal amount of time, in order to ensure the termination in a reasonable time. Finally, the parallel scheme is depicted in Fig. 3.

[Figure 3 about here.]

The whole genetic process (lines 2–23) may be repeated several times (called epochs) to enhance the results. Also, as mentioned above, the function `checkEnd` may depend on an iterations counter.

In order to efficiently exploit the hardware resources, all cores in each machine have been used. So, the number of workers corresponds to the number of cores multiplied by the number of machines minus one (kept for the master). As an example, if we use 10 machines with 16 cores, then we have 159 workers. This does not induce any modification in the code as `MP I` can manage several processes on a same machine as well as distributed on several machines. The deployment of the processes is depicted in Figure 4 where C_x is hardware core x , Mst is the master and W_x is worker x .

[Figure 4 about here.]

All the initial guesses of the model presented in this work have been obtained with this algorithm used on the Grid'5000 platform [42]. Our algorithm has been implemented in `python` and the `MP I` module `mpi4py` [43].

Although, as mentioned previously, the genetic process is a random process whose results and convergence time may vary from one execution to another, we have observed in our simulations that it is quite stable in practice. For the model based on 6 gray gases, the average computation time (over 10 executions) to find optimized initial guesses on a cluster of 10 machines with 319 workers is 2h49 with a standard deviation around 7min30 for a time limit of 3h00. Also, the average error of the obtained model is 3.51 % with a standard deviation of 0.038 %.

It is worth noting that, for a given case, the manual "trial-and-error" method can give satisfactory results and the genetic algorithm which allows to find the other initial guesses can improve in general the model accuracy, in at least 2.0%.

3.3 Discussion on the reconstruction results of the model parameters

The parameters (of the proposed model for 6 gray gases) reconstructed from the data of Tables 2 and 3, and based on the formulation given in Eqs. (36)-(38), are depicted in Fig. 5. Fig. 5(a) shows that the pressure absorption coefficients $\kappa_{p,k}$ have weak dependencies with the temperature and are strictly increasing functions of the temperature. Fig. 5(b) shows that $w_k[T]$ are strictly decreasing functions of the temperature. This property can be deduced from the relations (18)-(20). As shown below, the best solution is obtained when $\kappa_{p,k}$ have weak dependencies with the temperature. However, note also that, if we set as constraint in the inverse algorithm to seek constant coefficients $\kappa_{p,k}$, it does not converge. Without this constraint, it will converge and find the coefficients $\kappa_{p,k}$ presented in Fig. 5(a). It can be seen in Fig. 5(c) that $\sum_{k=1}^K w_k[T]$ for low temperatures T (between 400 K and 650 K) is higher than 1. We like to associate the weighting factors to the fraction of blackbody emission, which should be limited to 100%, but as stated before, the present model is above all a fitting model, so in this sense, we can accept that $\sum_{k=1}^K w_k[T]$ is higher than 1 for certain temperatures in exchange for consistently accurate results for the radiative transfer. As it will be seen after, even with the result of Fig. 5(c), the present model leads to accurate results.

[Figure 5 about here.]

3.4 Discussion on the model accuracy

For Case 1, Fig. 6 shows a comparison on S_r computed both with the present model, the WSGG model by Dorigon et al. (standard WSGG model) [15] and the LBL method. Fig. 7 shows the comparison on Q_r . Figs. 6(a) and 7(a) show that the standard WSGG model gives discrepancies with the reference LBL solution, by overpredicting the extrema of S_r and Q_r . A perfect agreement in the whole domain is observed between the solution of the present model and the reference. Figs. 6(b) and 7(b) show that the results of Case 1 are in nearly perfect agreement with those of the LBL method: the normalized errors on both S_r and Q_r are very low in the whole domain with (in %): $\delta S_{\max} = 1.12 \cdot 10^{-7}$, $\delta S_{\text{avg}} = 3.8 \cdot 10^{-8}$ and $\delta Q_{\max} = 0.05$, $\delta Q_{\text{avg}} = 0.02$.

[Figure 6 about here.]

[Figure 7 about here.]

For cases 2 to 17, Figs (8) and (9) show that the present model drastically reduce the errors of the standard WSGG model. For all the cases, δS_{\max} does not exceed 3.5%, whereas for the standard WSGG model, these errors vary up to 14.5% (five cases have errors higher than 10.0% and nine cases have errors between 5.0% and 10.0%). In the same way, δS_{avg} does not exceed 2.1%, whereas for the standard WSGG model these errors vary up to 8.0% (12 cases have errors between 2.0% and 8.0%). The accuracy of Q_r is also greatly improved with the new model. For all the cases, δQ_{\max} does not exceed 4.0% whereas for the standard WSGG model these errors vary up to 10.4% (8 cases have errors between 5.0% and 10.0%). Concerning δQ_{avg} , they are not so high for the standard WSGG model (less than 4.3%). Still, the same errors are less than 2.5% for the new model. Except for case 1 solved by inverse method, the normalized errors for S_r of the present model are rather uniform for all the cases. They are between 1.4% - 3.5% for δS_{\max} and 0.5% - 2.1% for δS_{avg} . The errors for Q_r are a little bit less uniform. They are between 0.7% - 4.1% for δQ_{\max} and 0.3% - 2.6% for δQ_{avg} .

Note that the standard WSGG model provides accurate results for the cases 4, 8 and 12, which have spatially non-constant profiles for the participating species mole fractions. For all these three cases, $\delta S_{\max} \leq 2.3\%$, $\delta S_{\text{avg}} \leq 1.0\%$, $\delta Q_{\max} \leq 1.6\%$ and $\delta Q_{\text{avg}} \leq 1.2\%$ for the model. These results are a little bit better than those of the new model. However, the standard WSGG model does not provide always accurate results for the cases which have spatially non-constant species concentrations profiles, as shown by the results for cases 13 to 17; for those, the present model is more accurate.

[Figure 8 about here.]

[Figure 9 about here.]

For the standard WSGG model, Fig. 8(a) shows that the errors δS_{\max} have a small increase with the length L (Cases 2 and 3 compared to case 1, Cases 6 and 7 compared to case 5, Cases 10 and 11 compared to case 9). For further study, Fig. 10 shows the maximum and average normalized errors on S_r and Q_r for high lengths L (3 m, 4 m and 5 m). As a similar behavior will be observed for the other cases, the errors are shown here for Case 1.

Figures 10(a) and 10(b) show that the normalized errors on S_r for the new model have a slight increase with these larger path lengths. For $L = 5$ m, δS_{\max} and δS_{avg} are of 5.3% and 3.7%, respectively. However, the normalized errors on Q_r increase considerably. For $L = 5$ m, δQ_{\max} and δQ_{avg} are of 14.1% and 7.9%, respectively (Figs. 10(c) and 10(d)). An improvement of the accuracy of Q_r for high lengths L will be investigated in future works.

[Figure 10 about here.]

Table 4 gives an overview of the model accuracy with the number K . Γ (defined by (39)) is specified in Table 4. It is observed that the best model accuracy is achieved with 6 gray gases and, as expected, for $K = 1$ the model has the highest

error (27.9%). Satisfactory results are however obtained with 2 gray gases (7.9%).

It is worth noting that most of the older WSGG versions are based on 4 gray gases because they probably achieve the most accurate solutions using this number of gray gases. In the present study, the parameters were determined for the model using 1 to 7 gray gases (see Table 4). As the model using 6 gray gases leads to the most accurate solutions, the values of the best initial guesses and $w_1(T^{\text{ref}})$ were given for 6 gray gases. The model using 4 gray gases has also a good accuracy (Γ is equal to 4.9% in Table 4). If the older WSGG versions are compared to the developed model for 4 gray gases, there is no loss in computational efficiency for applications. However, if the older WSGG versions are compared to the developed model using 6 gray gases, there is loss in computational efficiency for applications but in the same time, there is also gain in accuracy with the new model.

[Table 4 about here.]

3.5 Discussion about the present model in comparison to the RC-SLW model proposed by Bagder et al. [11]

The SLW model [10] is deservedly one of the most praised gas models, and is still undergoing improvements with new developments as in [11]. However, the development of new models should still be welcomed since no single model will be capable to be the best alternative for all users and applications.

The great advantage of the SLW model in comparison to the present model is that it can achieve highly accurate solutions by using a high number of gray gases but with attendant higher computational times. As stated in section 2.1, the present model is a homogenized model with effective parameters $\kappa_{p,k}$ and w_k . It is thus constructed in a different way in comparison to the SLW model. It is worth mentioning that even with one gray gas and one clear gas, the solution of the inverse problem (using the present model) for a given test case is in nearly perfect agreement with the one of the LBL method. However, this solution is not accurate for the test cases solved in forward calculation (in Table 4, Γ is 27.9% when $K = 1$). That's why, more gray gases are needed in the model to achieve accurate solutions for the test cases solved in forward calculations and, it is natural to find an optimal accuracy for a given (limited) value of the number K . In Table 4, it is shown that this optimal is obtained when $K = 6$ with $\Gamma = 3.5\%$. Table 4 also shows that the developed model achieves reasonably accurate solutions with as few as 3-5 gray gases: Γ is 6.2%, 4.9% and 3.7% for 3, 4 and 5 gray gases, respectively.

According to [11], the computational resource of the RC-SLW increases almost only linearly with the number of gray gases. When K gray gases are used, its computational time is nominally 1.5 K times that of the standard WSGG model

using one gray gas. One advantage of the present model is that the computational time is similar to that of the standard WSGG model. Thus, for a fixed precision Γ of Table 4, the RC-SLW model using the necessary number of gray gases to have this precision should be more time consuming than the present model. However, the present model is currently limited to the precision of $\Gamma = 3.5\%$ whereas the RC-SLW is not limited and can achieve highly accurate solutions (Γ less than 3.5%).

3.6 3D test case studied

Next, we show that the proposed model can be applied to a 3D geometry. The model was applied to the radiative transfer calculation of a CO₂-H₂O mixture on a rectangular parallelepiped domain of dimension 2 m × 2 m × 4 m. The domain has cold black walls at 400 K. A non-uniform gas temperature was considered and is symmetrical about the domain centerline:

$$T(\zeta) = (T_c - T_e) g(\zeta) + T_e \quad \text{with} \quad g(\zeta) = 1 - 3\zeta^2 + 2\zeta^3, \quad (43)$$

where ζ is the radial distance from the domain centerline and T_e is the temperature at $z = 4$ m (exit) equal to 800 K. The domain geometry is defined on Cartesian coordinate system (O, x, y, z) . The temperature outside the unit circular region is constant and equal to T_e . T_c is the temperature along the domain centerline, which is assumed to increase linearly from 400 K at $z = 0$ (inlet) to 1,800 K at $z = 0.375$ m, then decreases linearly to 800 K at the exit. A non-homogeneous gas mixture is studied with $Y_{\text{CO}_2}(\zeta) = g(\zeta) Y_c$ where Y_c is the mole fraction of this species along the centerline, which is assumed to increase linearly from 0 at the inlet to 0.1 at $z = 0.375$ m, then decreases linearly to 0 at the exit. The solution of the RTE for this test case was obtained using a Finite Volume Method (1) with high angular discretization and a regular spatial mesh composed of $32 \times 32 \times 64$ nodes. The 3D numerical method to solve the RTE (1) is provided in [44] and is not repeated here. The results presented below were obtained either with the LBL method based on HITEMP 2010, the developed model (for 6 gray gases) and the WSGG model by Dorigon et al. (standard WSGG model) [15] for comparison. S_r along the centerline (1 m, 1 m, z) and Q_r along line (2 m, 1 m, z) are shown in Figs 11 and 12. The maximum and average normalized errors on S_r and Q_r are specified in Figs 11(b) and 12(b). The present model show a better agreement with the reference solution for either S_r and Q_r compared to the standard WSGG model. The obtained results show that the present model is robust and can be applied to a 3D geometry.

[Figure 11 about here.]

[Figure 12 about here.]

4 Conclusions and future perspectives

A new model based on the principle of the Weighted-Sum-of-Gray-Gases (WSGG) model has been proposed in this study. In order to obtain a good accuracy, the pressure absorption coefficient of the new model needed to have a weakly dependence with the temperature. In the standard WSGG model, the weighting factor is expressed with polynomial functions of the temperature. In this work, it has not been predefined by a mathematical function. Mathematical properties on the model parameters have been obtained and we have shown that all the model parameters can be determined from only one of them, which in turn was reconstructed using an efficient inverse algorithm with the total radiative heat source S_r data obtained with the LBL method based on HITEMP 2010. By applying the inverse algorithm to a given test case, the results obtained are in nearly perfect agreement with those of the LBL method. It has been possible to apply this model to other test cases since the parameters obtained are functions of the temperature. Also, we developed an efficient algorithm which allows to find good initial guesses (of the model parameters), leading to an improved accuracy of the model.

Our methodology has been applied to reconstruct the model parameters for H_2O - CO_2 mixtures at atmospheric pressure with mole fraction ratio equal to two (representative of products of typical air-fired methane combustion), within the range of temperature between 400 K and 1,800 K and for thicknesses of the gas layer up to 5 m.

When the methodology is applied to several test cases (1D and 3D), this led to a greatly decrease in the relative errors on S_r and, on the radiative heat flux Q_r compared to that obtained with the standard WSGG model. The new model can be applied exactly the same way as the standard approaches of the WSGG model. Moreover, the computational time is similar to that of the standard WSGG model, making it attractive for CFD calculations.

The mole fraction ratio between H_2O and CO_2 is fixed to two. This is the major weakness of the WSGG model that cannot handle easily complex space-varying gas/soot mixtures. Currently, this limits considerably the impact of this study for applications. Also, it is worth noting that local instantaneous flame temperature can exceed 2,200 K even when burning in air. Such cases would be out of the range of applicability of the correlations and coefficients of the present model, obtained for temperatures up to 1,800 K. However, the proposed inverse methodology is not limited to the physical conditions considered in the present study, and can be applied to extend the model parameters to higher temperatures (even above 2,200 K) or to consider different gas compositions and operational pressures.

As perspectives, some improvements of the computational method of the present study will be addressed. Also, we plan to apply our model to other gas mixtures and more complex cases. The model parameters for higher temperatures (up to 2,500 K) will be studied. An improvement of the accuracy of Q_r for high lengths L (3 m to 5 m) will also be investigated.

Appendix A. Computation of the cost function's gradients

In this work, the expressions of the cost function's gradients over the parameters of interest are derived from the Lagrangian formulation and the adjoint state of the RTE. Then, they are introduced in the following.

A.1 Space functions and associated inner products

Let $L^2(\Sigma)$ be the space function which is square integrable on Σ . The associated inner product is:

$$\langle f | g \rangle_{\Sigma} = \int_{-1}^1 f(\mu) g(\mu) d\mu \text{ for all } f, g \in L^2(\Sigma).$$

Moreover, the $L^2(\mathcal{D})$ and $L^2(\mathcal{D} \times \Sigma)$ space functions are square integrable on \mathcal{D} and $\mathcal{D} \times \Sigma$. The two associated inner products are:

$$\begin{aligned} \langle f | g \rangle_{\mathcal{D}} &= \int_0^L f(x) g(x) dx \text{ and } \|f\|_{\mathcal{D}}^2 = \langle f | f \rangle_{\mathcal{D}} \text{ for all } f, g \in L^2(\mathcal{D}), \\ \langle f | g \rangle_{\mathcal{D}, \Sigma} &= \int_0^L \int_{-1}^1 f(x, \mu) g(x, \mu) d\mu dx \text{ for all } f, g \in L^2(\mathcal{D} \times \Sigma), \end{aligned}$$

in which $\|f\|_{\mathcal{D}}$ is the associated norm to $L^2(\mathcal{D})$.

The notations presented here are used in the following of this Appendix and in Appendix B.

A.2 State and observation equations

In this appendix, S_r computed with the present model and the LBL method are denoted by K and H , respectively. Then, the cost function (12) can be written as:

$$J(\theta) = \frac{1}{2} \left\| \frac{K(\theta) - H}{H_{\max}} \right\|_{\mathcal{D}}^2, \quad (44)$$

where $K(\theta)$ in Eq. (44) is the observation equation defined as S_r over the parameter θ . It can be also written as:

$$K(\theta)(x) = \sum_{k=1}^K (\Psi I_k)(x) - \Phi(x), \quad (45)$$

with

$$(\Psi I_k)(x) = 2\pi \kappa_{p,k}(x) p_a(x) \int_{-1}^1 I_k(x, \mu) d\mu \text{ and } \Phi(x) = 4\pi \kappa_P(x) I_b[T(x)]. \quad (46)$$

The terms $\mathcal{R}_k^+(\theta, I_k^+)$ and $\mathcal{R}_k^-(\theta, I_k^-)$ are denoted by Eqs. (2) and (3), respectively. Then, the state equation is defined by:

$$\mathcal{R}(\theta, I_1, I_2, \dots, I_K) = \left\{ \mathcal{R}_k^+(\theta, I_k^+), \mathcal{R}_k^-(\theta, I_k^-) \right\}_{k=1}^K. \quad (47)$$

The cost function J (44) is minimized according to the inverse algorithm when Eq. (47) is satisfied [30].

A.3 Lagrangian expression and adjoint equations model

In the L^2 function space, the Lagrangian expression is stated as [30, 36]:

$$\mathcal{L}(\theta, I_1, I_2, \dots, I_K, \tilde{I}_1, \tilde{I}_2, \dots, \tilde{I}_K) = \frac{1}{2} \left\| \frac{\sum_{k=1}^K (\Psi I_k) - \Phi - H}{H_{\max}} \right\|_{\mathcal{D}}^2 + \sum_{k=1}^K \left\langle \tilde{I}_k \middle| \mathcal{R}_k \right\rangle_{\mathcal{D}, \Sigma}, \quad (48)$$

where the Lagrangian multipliers are functions defined by: $\tilde{I}_k(x, \mu)$ with $(x, \mu) \in \mathcal{D} \times \Sigma$ for $k = 1, \dots, K$. They are the adjoint state of partial radiative intensity I_k ($k = 1, \dots, K$). It is worth noting that if I_k ($k = 1, \dots, K$) are solutions of the state equation (47) for the θ parameter, then the following equation is satisfied:

$$\mathcal{L}(\theta, I_1(\theta), I_2(\theta), \dots, I_K(\theta), \tilde{I}_1, \tilde{I}_2, \dots, \tilde{I}_K) = J(\theta) \text{ for all } \tilde{I}_k, \quad k = 1, \dots, K. \quad (49)$$

Eq. (49) leads to obtain the adjoint equations model. By deriving Eq. (49), it follows:

$$J'(\theta) \delta\theta = \frac{\partial \mathcal{L}(\theta, I_1, I_2, \dots, I_K, \tilde{I}_1, \tilde{I}_2, \dots, \tilde{I}_K)}{\partial \theta} \delta\theta + \sum_{k=1}^K \frac{\partial \mathcal{L}(\theta, I_1, I_2, \dots, I_K, \tilde{I}_1, \tilde{I}_2, \dots, \tilde{I}_K)}{\partial I_k} \frac{\partial I_k(\theta)}{\partial \theta} \delta\theta. \quad (50)$$

Then, the adjoint variables satisfy [30, 36]:

$$\sum_{k=1}^K \frac{\partial \mathcal{L}(\theta, I_1, I_2, \dots, I_K, \tilde{I}_1, \tilde{I}_2, \dots, \tilde{I}_K)}{\partial I_k} \delta I_k = 1. \quad (51)$$

The sensitivity directions δI_k are formulated as:

$$\delta I_k = \frac{\partial I_k(\theta)}{\partial \theta} \delta\theta. \quad (52)$$

Equation (50) is then reduced to:

$$J'(\theta) \delta\theta \equiv \left\langle \nabla J(\theta) \middle| \delta\theta \right\rangle_{\mathcal{D}} = \frac{\partial \mathcal{L}(\theta, I_1, I_2, \dots, I_K, \tilde{I}_1, \tilde{I}_2, \dots, \tilde{I}_K)}{\partial \theta} \delta\theta. \quad (53)$$

Combining Eq. (48) with Eq. (51), it yields:

$$\sum_{k=1}^K \left\langle \frac{\sum_{i=1}^K (\Psi I_i) - \Phi - H}{H_{\max}} \middle| \frac{(\Psi \delta I_k)}{H_{\max}} \right\rangle_{\mathcal{D}} + \sum_{k=1}^K \left\langle \tilde{I}_k \middle| \frac{\partial \mathcal{R}_k}{\partial I_k} \delta I_k \right\rangle_{\mathcal{D}, \Sigma} = 0. \quad (54)$$

Using Eq. (45), $\sum_{i=1}^K (\Psi I_i) - \Phi$ is replaced by K in the first term of Eq. (54). Eq. (54) has to be satisfied for all δI_k .

Then, for each sensitivity directions:

$$\left\langle \frac{K - H}{H_{\max}} \middle| \frac{(\Psi \delta I_k)}{H_{\max}} \right\rangle_{\mathcal{D}} + \left\langle \tilde{I}_k \middle| \frac{\partial \mathcal{R}_k}{\partial I_k} \delta I_k \right\rangle_{\mathcal{D}, \Sigma} = 0. \quad (55)$$

The adjoint operator is denoted with the subscript (*). Then, Eq. (55) leads to:

$$\left\langle \left(\frac{\partial \mathcal{R}_k}{\partial I_k} \right)^* \tilde{I}_k \middle| \delta I_k \right\rangle_{\mathcal{D}, \Sigma} + \left\langle \frac{\Psi^*(K - H)}{H_{\max}^2} \middle| \delta I_k \right\rangle_{\mathcal{D}, \Sigma} = 0. \quad (56)$$

The partial adjoint radiative intensity at the spatial position x , in the μ direction, is defined as:

$$\tilde{I}_k(x, \mu) = \left\{ \begin{array}{ll} \tilde{I}_k^+(x, \mu) & \mu \in \Sigma^+ \\ \tilde{I}_k^-(x, -\mu) & \mu \in \Sigma^- \end{array} \right\} \text{ for } k = 1, \dots, K.$$

Replacing \mathcal{R}_k defined by Eq. (47) in Eq. (56) and using Appendix C, the following adjoint equations model is obtained:

$$\mu \frac{\partial \tilde{I}_k^-(x, -\mu)}{\partial x} + \kappa_{p,k}(x) p_a(x) \left\{ \tilde{I}_k^-(x, -\mu) + 2\pi \frac{(K(x) - H(x))}{H_{\max}^2} \right\} = 0, \quad (57)$$

$$-\mu \frac{\partial \tilde{I}_k^+(x, \mu)}{\partial x} + \kappa_{p,k}(x) p_a(x) \left\{ \tilde{I}_k^+(x, \mu) + 2\pi \frac{(K(x) - H(x))}{H_{\max}^2} \right\} = 0, \quad (58)$$

for $\mu \in \Sigma^+$ and $k = 1, \dots, K$. For convenience, the μ direction was changed by $-\mu$ in the above equations.

The partial adjoint radiative intensity satisfy the following boundary conditions:

$$\tilde{I}_k^-(x = 0, -\mu) = 0 \quad ; \quad \tilde{I}_k^+(x = L, \mu) = 0. \quad (59)$$

for $\mu \in \Sigma^+$ and $k = 1, \dots, K$.

A.4 Expressions of the cost function's gradients

The differentiation of the Lagrangian expression according to θ in direction $\delta\theta$ leads to:

$$\frac{\partial \mathcal{L}(\theta, I_1, I_2, \dots, I_K, \tilde{I}_1, \tilde{I}_2, \dots, \tilde{I}_K)}{\partial \theta} \delta\theta = \frac{\partial J(\theta)}{\partial \theta} \delta\theta + \sum_{k=1}^K \left\langle \tilde{I}_k \left| \frac{\partial \mathcal{R}_k}{\partial \theta} \delta\theta \right. \right\rangle_{\mathcal{D}, \Sigma}. \quad (60)$$

Using Eq. (53), it follows:

$$\left\langle \nabla J(\theta) \middle| \delta\theta \right\rangle_{\mathcal{D}} = \left\langle \frac{K(\theta) - H}{H_{\max}} \middle| \frac{1}{H_{\max}} \frac{\partial R(\theta)}{\partial \theta} \delta\theta \right\rangle_{\mathcal{D}} + \sum_{k=1}^K \left\langle \tilde{I}_k \left| \frac{\partial \mathcal{R}_k}{\partial \theta} \delta\theta \right. \right\rangle_{\mathcal{D}, \Sigma}. \quad (61)$$

Equation (61) allows to compute the cost function's gradients. Applying Eq. (61) to $\theta = \kappa_{p,i}$, it follows that:

$$\begin{aligned} \left\langle \nabla J(\kappa_{p,i}) \middle| \delta\kappa_{p,i} \right\rangle_{\mathcal{D}} &= \left\langle \frac{K - H}{H_{\max}^2} \middle| 2\pi p_a \int_{-1}^1 I_i(\cdot, \mu) d\mu - 4\pi p_a w_i I_b[T] \delta\kappa_{p,i} \right\rangle_{\mathcal{D}} \\ &+ \left\langle \tilde{I}_i \middle| p_a I_i - p_a \left\{ w_i I_b[T] \right\} \delta\kappa_{p,i} \right\rangle_{\mathcal{D}, \Sigma}. \end{aligned} \quad (62)$$

Then, the cost function's gradient over $\kappa_{p,i}$ is:

$$\begin{aligned} \nabla J(\kappa_{p,i})(x) &= 2\pi \frac{(K(x) - H(x))}{H_{\max}^2} p_a(x) \left(\int_{-1}^1 I_i(x, \mu) d\mu - 2 w_i(x) I_b[T(x)] \right) \\ &+ p_a(x) \int_{-1}^1 \tilde{I}_i(x, \mu) I_i(x, \mu) d\mu - p_a(x) w_i(x) I_b[T(x)] \int_{-1}^1 \tilde{I}_i(x, \mu) d\mu. \end{aligned} \quad (63)$$

Applying Eq. (61) to $\theta = w_i$ for $i = 1, \dots, K$, it follows that:

$$\left\langle \nabla J(w_i) \middle| \delta w_i \right\rangle_{\mathcal{D}} = \left\langle \frac{K - H}{H_{\max}^2} \middle| -4\pi \kappa_{p,i} p_a I_b[T] \delta w_i \right\rangle_{\mathcal{D}} - \left\langle \tilde{I}_i \middle| \kappa_{p,i} p_a I_b[T] \delta w_i \right\rangle_{\mathcal{D}, \Sigma}. \quad (64)$$

Then, the cost function's gradient over w_i is:

$$\nabla J(w_i)(x) = -\kappa_{p,i}(x) p_a(x) I_b[T(x)] \left(4\pi \frac{(K(x) - H(x))}{H_{\max}^2} + \int_{-1}^1 \tilde{I}_i(x, \mu) d\mu \right). \quad (65)$$

A.5 Simplified expressions for the cost function's gradients

From (63), (65) and for a better convergence of the inverse algorithm [30], the spatially non-constant parameters $\kappa_{p,i}$ and w_i can be computed using simplified expressions for the cost function's gradients as:

$$\nabla J(w_i)(x) = -\frac{(K(x) - H(x))}{H_{\max}^2} \quad \text{and} \quad \nabla J(\kappa_{p,i}) = -\nabla J(w_i) \quad \text{for } i = 1, \dots, K. \quad (66)$$

It is worth noting that, to compute these simplified expressions, the adjoint equations model has not to be solved.

Appendix B. Calculations of adjoint operators

Let $\psi \in L^2(\mathcal{D})$. From (45), it yields:

$$\begin{aligned} \left\langle \psi \left| (\Psi \delta I_k) \right. \right\rangle_{\mathcal{D}} &= 2\pi \int_{\mathcal{D}} \psi(x) \kappa_{p,k}(x) p_a(x) \int_{-1}^1 \delta I_k(x, \mu) d\mu dx \\ &= 2\pi \int_{\mathcal{D}} \int_{-1}^1 \kappa_{p,k}(x) p_a(x) \psi(x) \delta I_k(x, \mu) d\mu dx = \left\langle \Psi^* \psi \left| \delta I_k \right. \right\rangle_{\mathcal{D}, \Sigma}. \end{aligned} \quad (67)$$

with

$$(\Psi^* \psi)(x) = 2\pi \kappa_{p,k}(x) p_a(x) \psi(x). \quad (68)$$

Appendix C. Mathematical properties on the model parameters

After convergence, the relation (13) leads to:

$$\boldsymbol{\theta} = \boldsymbol{\theta}^{(0)} + \Delta\boldsymbol{\theta}, \quad (69)$$

where $\boldsymbol{\theta}^{(0)}$ is the initial guess vector, $\boldsymbol{\theta}$ is the converged solution and $\Delta\boldsymbol{\theta}$ is the convergence error. The relation (69) can be written with respect to $\kappa_{p,k}$ and w_k ($k = 1, \dots, K$) as:

$$\kappa_{p,k}(x) = \kappa_{p,k}^{(0)} + \Delta\kappa_p(x) \quad \text{and} \quad w_k(x) = w_k^{(0)} + \Delta w(x), \quad (70)$$

where $\Delta\kappa_p$ and Δw are convergence errors. They do not depend on the index k since the cost function's gradients with respect to $\kappa_{p,k}$ and w_k given by Eqs. (14) do not depend on the index k . Then, the relations (70) lead to:

$$\kappa_{p,k}(x) - \kappa_{p,1}(x) = \kappa_{p,k}^{(0)} - \kappa_{p,1}^{(0)} \quad \forall 2 \leq k \leq K, \quad (71)$$

$$w_k(x) - w_1(x) = w_k^{(0)} - w_1^{(0)} \quad \forall 2 \leq k \leq K, \quad (72)$$

From the relations (13), (15), (16), (17), (69) and (70), we obtain:

$$\kappa_{p,k}(x) = \kappa_{p,k}^{(0)} + \Delta\kappa_p(x) \quad \text{and} \quad w_k(x) = w_k^{(0)} - L p_a(x) \Delta\kappa_p(x) \quad \forall 1 \leq k \leq K, \quad (73)$$

where L is the domain length and p_a is the sum of the partial pressures of the chemical species. By multiplying the first relation of (73) by $L p_a(x)$ and summing the two relations for the index k set to 1, it follows:

$$L p_a(x) \kappa_{p,1}(x) + w_1(x) = L p_a(x) \kappa_{p,1}^{(0)} + w_1^{(0)}. \quad (74)$$

Note that the relation (74) is dimensionally consistent since the coefficients $w_1(x)$ and $w_1^{(0)}$ are dimensionless and the coefficients $L p_a(x) \kappa_{p,1}(x)$ and $L p_a(x) \kappa_{p,1}^{(0)}$ are also dimensionless ($\text{m} \cdot \text{atm} \cdot (\text{atm} \cdot \text{m})^{-1}$).

References

- [1] Goody RM, Yung YL, Atmospheric Radiation: Theoretical Basis. 2nd ed., Oxford University Press. 1995.
- [2] Modest MF, Haworth DC, Radiative Heat Transfer in Turbulent Combustion Systems: Theory and Applications. Springer, New-York. 2016.
- [3] Liu F, Consalvi JL, Coelho PJ, Andre F, Gu M, Solovjov V, Webb BW. The impact of radiative heat transfer in combustion processes and its modeling - with a focus on turbulent flames, Fuel 2020; 281: 118555.
- [4] Solovjov VP, Webb BW, André F, Radiative Properties of Gases, Handbook of Thermal Science and Engineering, 1069-1141. Springer, New-York. 2018.
- [5] Modest MF, Mazumder S, Radiative Heat Transfer. 4th. ed. New-York: Academic Press. 2022.
- [6] Hottel HC. Radiant-Heat Transmission. In Heat Transmission, 3rd ed., Ch.4, W.H. McAdams, ed., McGraw-Hill, New York, 1954.
- [7] Hottel HC, Sarofim AF, Radiative Transfer, McGraw-Hill, New York, 1967.
- [8] Modest MF, The weighted-sum-of-gray-gases model for arbitrary solution methods in radiative transfer, J. Heat Transfer 1991; 113(3): 650-656.
- [9] Fraga GC, Silva FR, Zanin LGB, da Fonseca RJC, França FHR, Centeno FR, A comprehensive evaluation of the WSGG model for air- and oxy-fuel combustion conditions through three-dimensional calculations, Fire Saf. J. 2021; 125:103433.
- [10] Webb BW, Solovjov VP, André F, The spectral line weighted-sum-of-gray-gases (SLW) model for prediction of radiative transfer in molecular gases, Advances in Heat Transfer 2019, Elsevier.
- [11] Badger J, Webb BW, Solovjov VP, An Exploration of Advanced SLW Modeling Approaches in Comprehensive Combustion Predictions, CST 2022; 194(2): 225-241.
- [12] Modest MF, Zhang H, The full-spectrum correlated- k distribution for thermal radiation from molecular gas-particulate mixtures, J. Heat Transfer 2002; 124(1): 30-38.

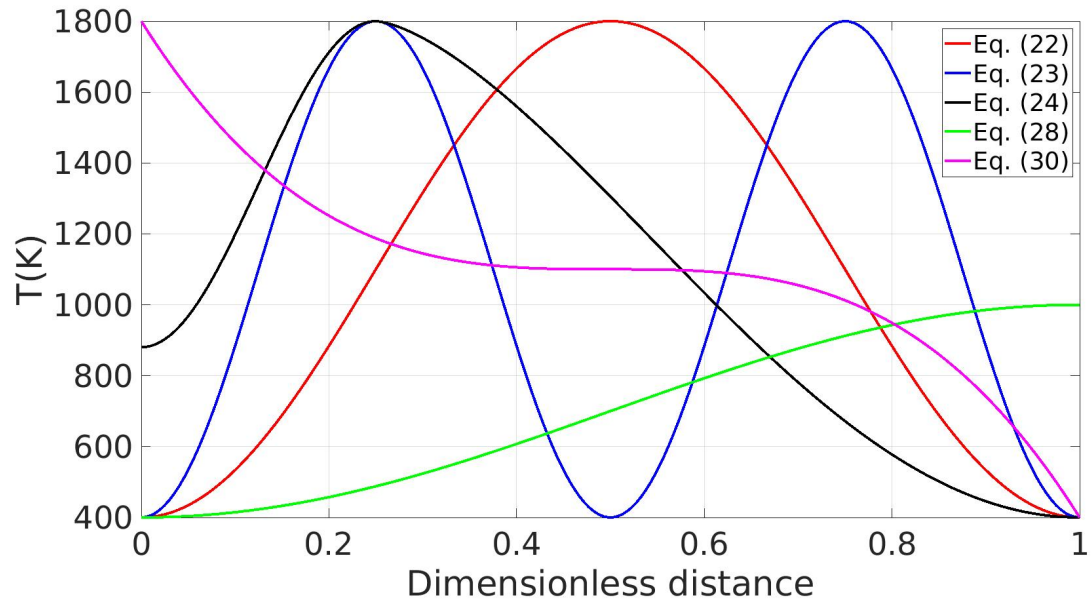
- [13] Rothman LS, Gordon IE, Barber RJ, Dothe H, Gamache RR, Goldman A, Perevalov VI, Tashkun SA, Tennyson J, HITEMP, the high-temperature molecular spectroscopic database, *J. Quant. Spectrosc. Radiat. Transf.* 2010; 111(15): 2139-2150.
- [14] Krishnamoorthy G, A new weighted-sum-of-gray-gases model for CO₂-H₂O gas mixtures, *Int. Comm. Heat Mass Transf.* 2010; 37(9): 1182-1186.
- [15] Dorigon LJ, Duciak G, Brittes R, Cassol F, Galarca M, Franca FHR. WSGG correlations based on HITEMP2010 for computation of thermal radiation in non-isothermal, non-homogeneous H₂O/CO₂ mixtures, *Int. J. Heat Mass Transf.* 2013; 64: 863-873.
- [16] Yin C, Refined weighted sum of gray gases model for air-fuel combustion and its impacts, *Energy & Fuels* 2013; 27(10): 6287-6294.
- [17] Bordbar MH, Wechel G, Hyppanen T. A line by line based weighted sum of gray gases model for inhomogeneous CO₂-H₂O mixture in oxy-fired combustion, *Combust. Flame* 2014; 161: 2435-2445.
- [18] Kangwanpongpan T, França FHR, da Silva RC, Schneider PS, Krautz HJ, New correlations for the weighted-sum-of-gray-gases model in oxy-fuel conditions based on HITEMP 2010 database, *Int. J. Heat Mass Transf.* 2012, 55(25):7419-7433.
- [19] Selhorst AHB, Fraga GC, Coelho FR, Bordbar H, França FHR, A compact WSGG formulation to account for inhomogeneity of H₂O-CO₂ mixtures in combustion systems, *ASME J. Heat Transfer* 2022; 144(7): 071301.
- [20] Kez V, Consalvi JL, Liu F, Koch M, Hatzfeld O, Kneer R, Development of a Weighted-Sum-of-Gray-Gases Model for Modeling Radiative Heat Transfer in Coal-Fired Oxy-Fuel Boilers, Conference: 9th International Symposium on Radiative Transfer, RAD-19. At: Athens, Greece, 3 - 7 June 2019.
- [21] Coelho FR, Fraga GC, França FHR, Generation of new WSGG correlations and analysis on the importance of considering transparent windows for soot, Conference: 9th International Symposium on Radiative Transfer, RAD-19. At: Athens, Greece, 3 - 7 June 2019.
- [22] Shan S, Zhou Z, Chen L, Wang Z, Cen K, New weighted-sum-of-gray-gases model for typical pressurized oxy-fuel conditions, *Int. J. Energy Res.* 2017; 41(15): 2576-2595.
- [23] Coelho FR, França FHR WSGG correlations based on HITEMP2010 for gas mixtures of H₂O and CO₂ in high total pressure conditions, *Int. J. Heat Mass Transfer* 2018; 127: 105-114.

- [24] Shan S, Qian B, Zhou Z, Wang Z, Cen K, New pressurized WSGG model and the effect of pressure on the radiation heat transfer of H₂O/CO₂ gas mixtures, *Int. J. Heat Mass Transfer* 2018; 121: 999–1010.
- [25] Wang B, Xuan Y, An improved WSGG model for exhaust gases of aero engines within broader ranges of temperature and pressure variations, *Int. J. Heat Mass Transfer* 2019; 136:1299–1310.
- [26] Zhou y, Duan R, Zhu X, Wu J, Ma J, Li X, Wang Q, An improved model to calculate radiative heat transfer in hot combustion gases, *Combust. Theory Model.* 2020: 1-23.
- [27] Guo J, Li X, Huang X, Liu Z, Zheng C, A full spectrum *k*-distribution based weighted-sum-of-gray-gases model for oxy-fuel combustion, *Int. J. Heat Mass Transf.* 2015; 90: 218-226.
- [28] Guo J, Hu F, Luo W, Li P, Liu Z, A full spectrum *k*-distribution based non-gray radiative property model for fly ash particles, *Int. J. Heat Mass Transf.* 2018; 118: 103-115.
- [29] Guo J, Shen L, Wan J, Li P, Liu Z, A full spectrum *k*-distribution-based weighted-sum-of-gray-gases model for pressurized oxy-fuel combustion, *Int. J. Energy Res.* 2020; 45(2): 3410-3420.
- [30] Asllanaj F, França FHR, Roche JR, da Fonseca RJC, Botella O, New gas radiation model based on the principle of weighted sum of gray gases. Application to CO₂-H₂O mixtures at high temperature, *Numer. Heat Transf. B* 2023.
- [31] Chu H, Liu F, Consalvi JL, Relationship between the spectral line based weighted-sum-of-gray-gases model and the full spectrum *k*-distribution model, *J. Quant. Spectrosc. Radiat. Transf.* 2014; 143:111-120.
- [32] Modest MF. The Treatment of Nongray Properties in Radiative Heat Transfer - From Past to Present, *J. Heat Transfer* 2013; 135(6): 4023596.
- [33] Coelho FR and Franca FHR. WSGG correlations based on HITEMP2010 for gas mixtures of H₂O and CO₂ in high total pressure conditions, *Int. J. Heat Mass Transf.* 2018; 127: 105-114.
- [34] Asllanaj F, Contassot-Vivier S, Botella O, Franca FHR. Numerical solutions of radiative heat transfer in combustion systems using a parallel modified discrete ordinates method and several recent formulations of WSGG model, *J. Quant. Spectrosc. Radiat. Transfer* 2021; 274: 107863.
- [35] Nocedal J, Wright S, *Numerical Optimization: New-York, Springer.* 1999.
- [36] J. F. Bonnans, J. C. Gilbert, C. Lemarechal, and C. A. Sagastizabal, 2016, *Numerical Optimization Theoretical and Practical Aspects.* Springer Sciences and Business Media.

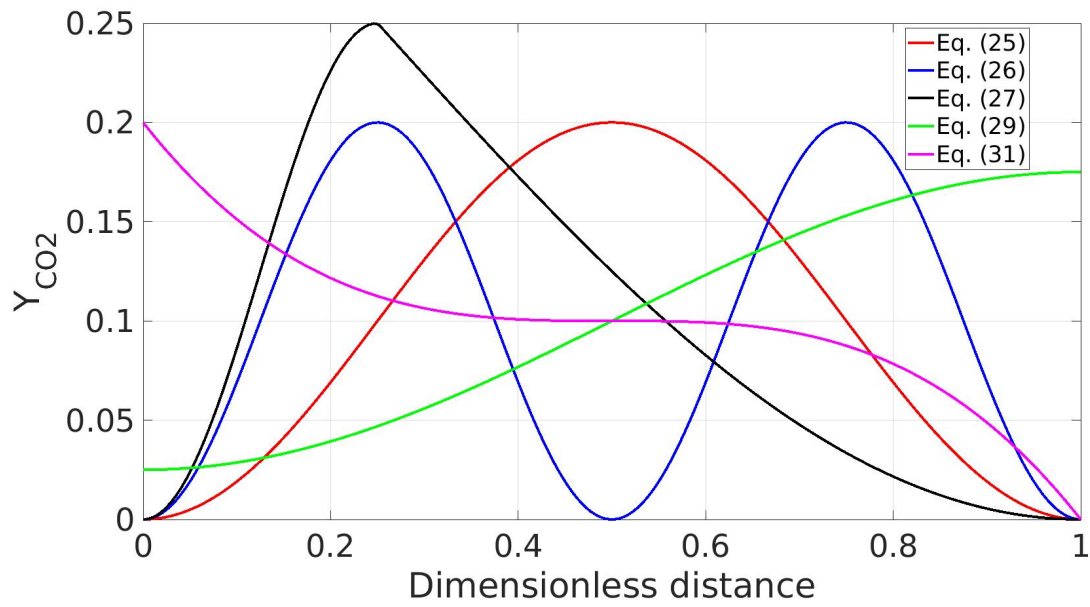
- [37] Andre F, Coelho FR, Consalvi JL, Franca FHR, Galtier M, Nmira F, Solovjov VP, Webb BW. Accuracy of engineering methods for radiative transfer in CO₂-H₂O mixtures at high temperature. Conference: 9th International Symposium on Radiative Transfer, RAD-19. At: Athens, Greece, 3 - 7 June 2019.
- [38] Katoch S, Chauhan SS, Kumar V, A review on genetic algorithm: past, present, future, *Multimed. Tools Appl.* 2021; 80(5): 8091-8126.
- [39] Storn R, Price K, Differential evolution – a simple and efficient heuristic for global optimization over continuous spaces, *J. Glob. Optim.* 1997; 11(4): 341-359.
- [40] Buhry L, Saïghi S, Giremus A, Grivel E, Renaud S, Automated tuning of analog neuromimetic integrated circuits, Conference BioCAS, 13-16, 2009.
- [41] Carvalho NA, Contassot-Vivier S, Buhry L, Martinez D, Simulation of large scale neural models with event-driven connectivity generation, *Front. Neuroinform.* 2020.
- [42] Balouek D et al., Adding Virtualization Capabilities to the Grid'5000 Testbed. *Cloud Computing and Services Science*, Springer International Publishing, Communications in Computer and Information Science, 367, 3-20, 2013.
- [43] Dalcin L, Fang YLL, mpi4py: Status Update After 12 Years of Development, *Comput. Sci. Eng.* 2021; 23(4): 47-54.
- [44] Fraga GC, H. Bordbar, S. Hostikka, França FHR. Benchmark Solutions of Three-Dimensional Radiative Transfer in Nongray Media Using Line-by-Line Integration, *J. Heat Transfer* 2020; 142: 034501-1.

List of Figures

1	Profiles of temperature and CO ₂ mole fraction.	30
2	Convergence of the cost function $J(w_1)$ according to the iteration number.	31
3	Parallel scheme of the genetic algorithm	32
4	Example of processes deployment over 3 machines with 4 cores.	33
5	Parameters for the 6 gray gases model.	34
6	Comparison on S_r obtained with the present model (for 6 gray gases), standard WSGG model and LBL method for Case 1.	35
7	Comparison on Q_r obtained with the present model (for 6 gray gases), standard WSGG model and LBL method for Case 1.	36
8	Maximum (δS_{\max}) and average (δS_{avg}) normalized errors on S_r obtained with the present model (for 6 gray gases) and standard WSGG model for the cases reported in Table 1, according to the LBL solution.	37
9	Maximum (δQ_{\max}) and average (δQ_{avg}) normalized errors on Q_r obtained with the present model (for 6 gray gases) and standard WSGG model for the cases reported in Table 1, according to the LBL solution.	38
10	Maximum ($\delta S_{\max} - \delta Q_{\max}$) and average ($\delta S_{\text{avg}} - \delta Q_{\text{avg}}$) normalized errors on S_r and Q_r obtained with the present model (for 6 gray gases) and standard WSGG model for the last three cases reported in Table 1, according to the LBL solution.	39
11	Comparison on S_r obtained with the present model (for 6 gray gases), standard WSGG model and LBL method for 3D Case with non-homogeneous gas mixture [44].	40
12	Comparison on Q_r obtained with the present model (for 6 gray gases), standard WSGG model and LBL method for 3D Case with non-homogeneous gas mixture [44].	41



(a) Temperature profiles.



(b) CO_2 mole fraction profiles.

Figure 1: Profiles of temperature and CO_2 mole fraction.

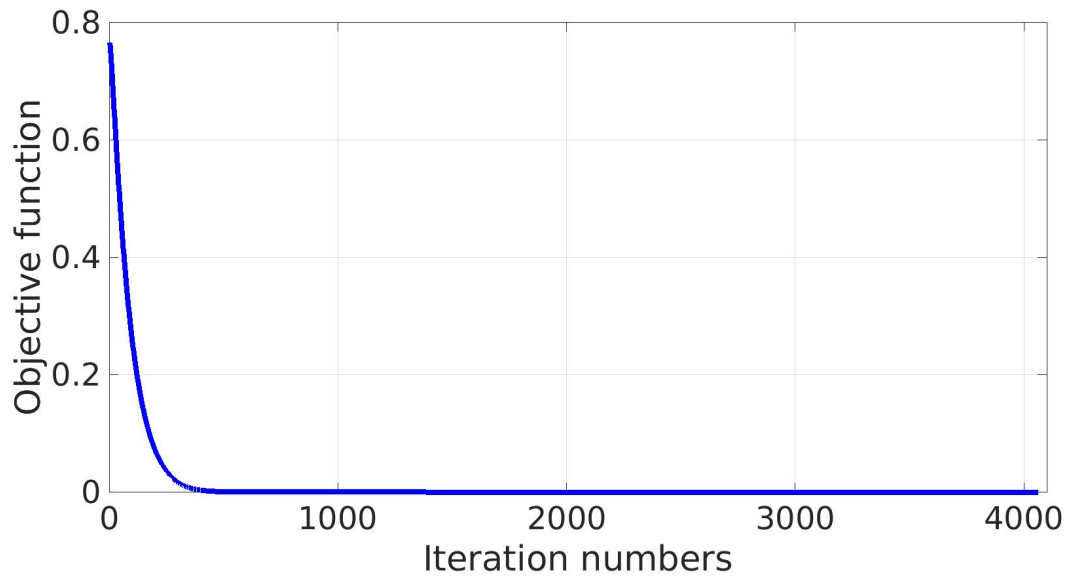


Figure 2: Convergence of the cost function $J(w_1)$ according to the iteration number.


```

1 for p in nbProcs do in parallel // Parallel loop over all the processes
2   finished ← false // Boolean indicating whether the genetic algorithm has finished or not
3   if p = 0 then // Master processus (number 0)
4     InitializePopulation() // Builds the first population of parameters vectors
5     errors ← distributeWork() // Distribution of the vectors to the workers and retrieving of the errors
6     while not finished do // Iterations of the genetic algorithm
7       best ← extractBest(errors) // Extracts the best vector with minimal error
8       differentiateAndMix(best) // Applies Eqs. (40) and (41)
9       errors ← distributeWork() // Distributes the vectors to the workers and gathers the errors
10      selection(errors) // Applies Eq. (42)
11      finished ← checkEnd(errors) // Checks whether the GA has finished
12    endwhile
13    broadcastEnd() // Sends the end signal to the workers
14    best ← extractBest(errors) // Extracts the final best vector
15  else // Workers processes
16    while not finished do // Iterations of the genetic algorithm
17      msg ← recvFromMaster() // Message reception from the master
18      if isEndMsg(msg) then // Checks whether the received msg is the end signal
19        finished ← true
20      else
21        error ← process(msg) // Executes the simulation with the parameters in msg
22        sendToMaster(error) // Sends back the obtained error to the master
23      endif
24    endwhile
25  endif
26 endfor

```

Figure 3: Parallel scheme of the differential evolution genetic algorithm used to find good initial guesses.

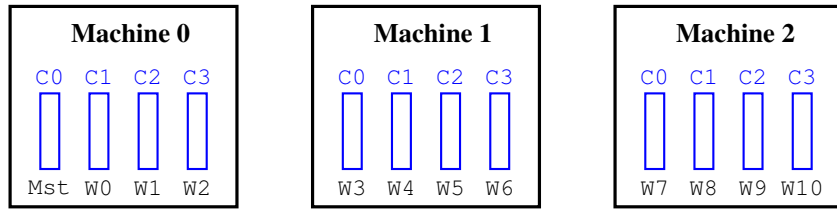
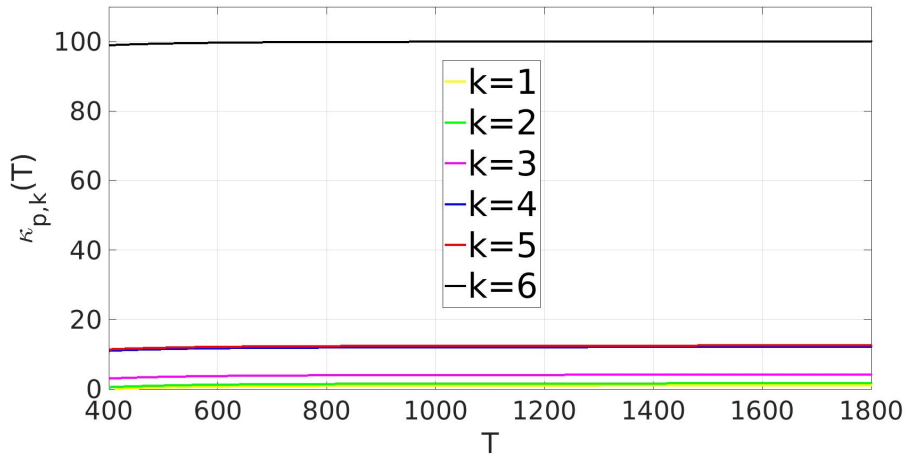
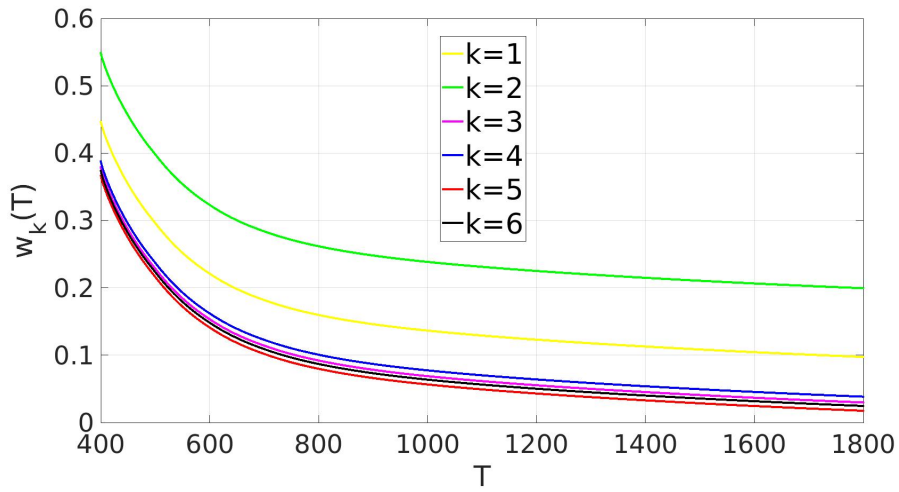


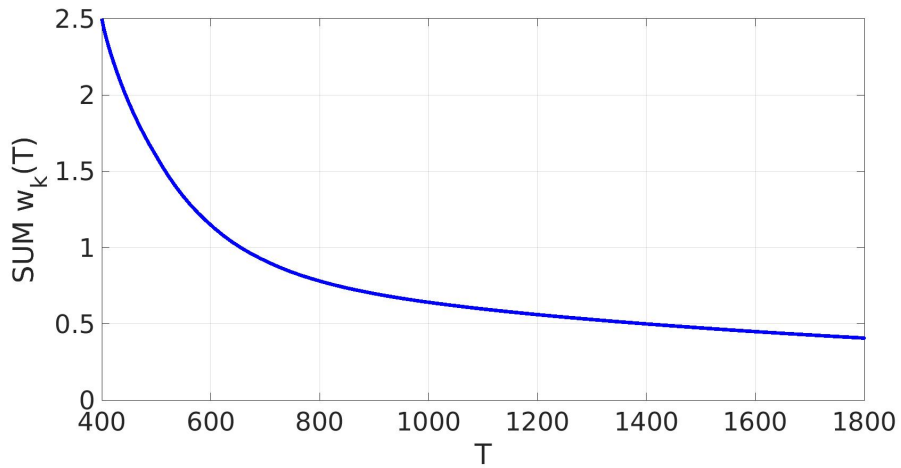
Figure 4: Example of processes deployment over 3 machines with 4 cores.



(a) $\kappa_{p,k}(T)$ profiles.

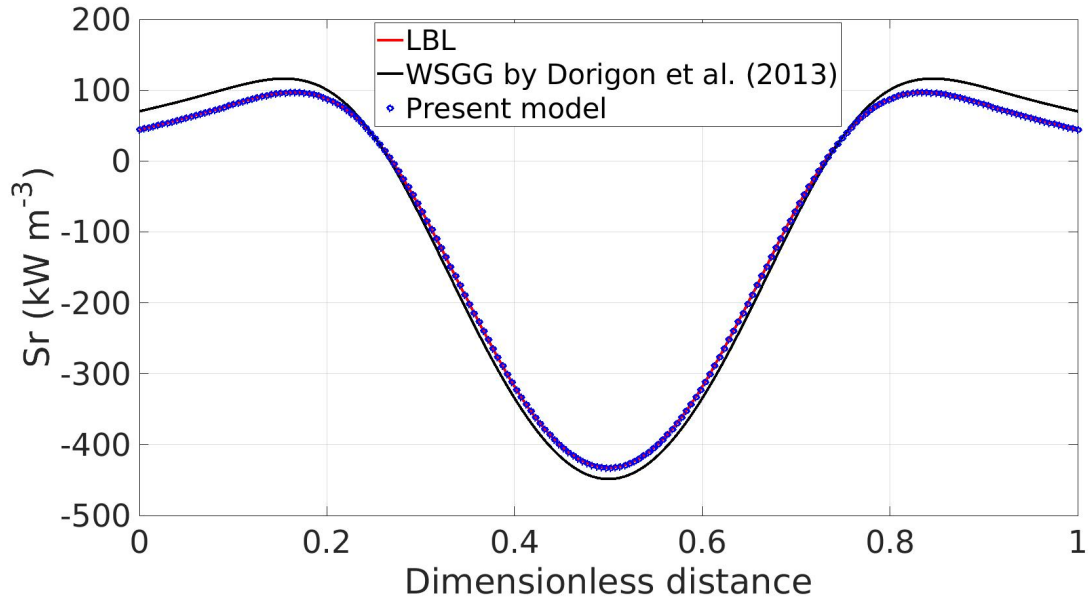


(b) $w_k(T)$ profiles.

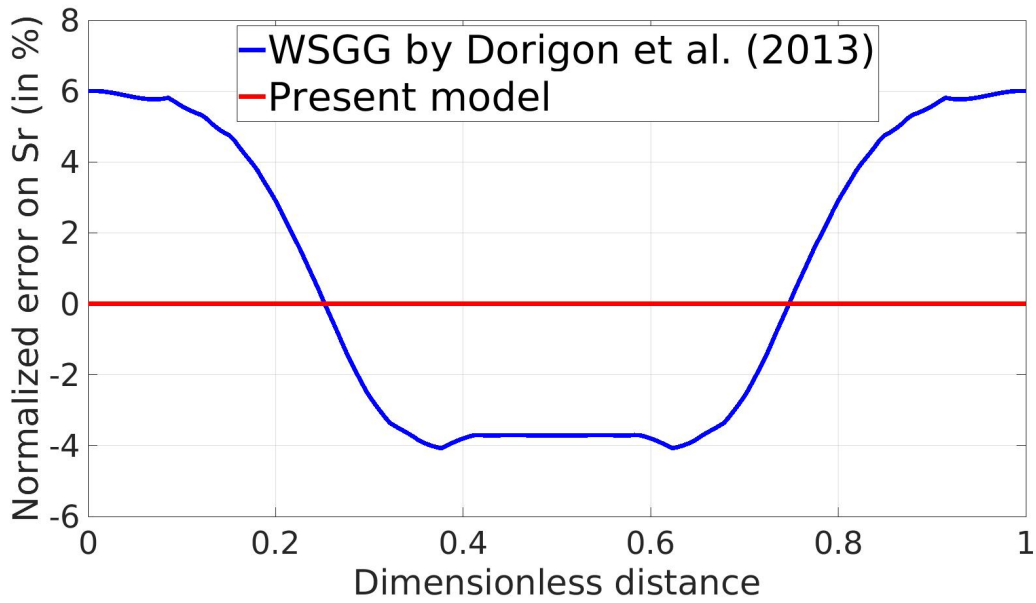


(c) $\sum_{k=1}^K w_k(T)$.

Figure 5: Parameters for the 6 gray gases model.



(a) Total radiative heat source S_r for Case 1.



(b) Normalized error on S_r for Case 1.

Figure 6: Comparison on S_r obtained with the present model (for 6 gray gases), standard WSGG model and LBL method for Case 1.

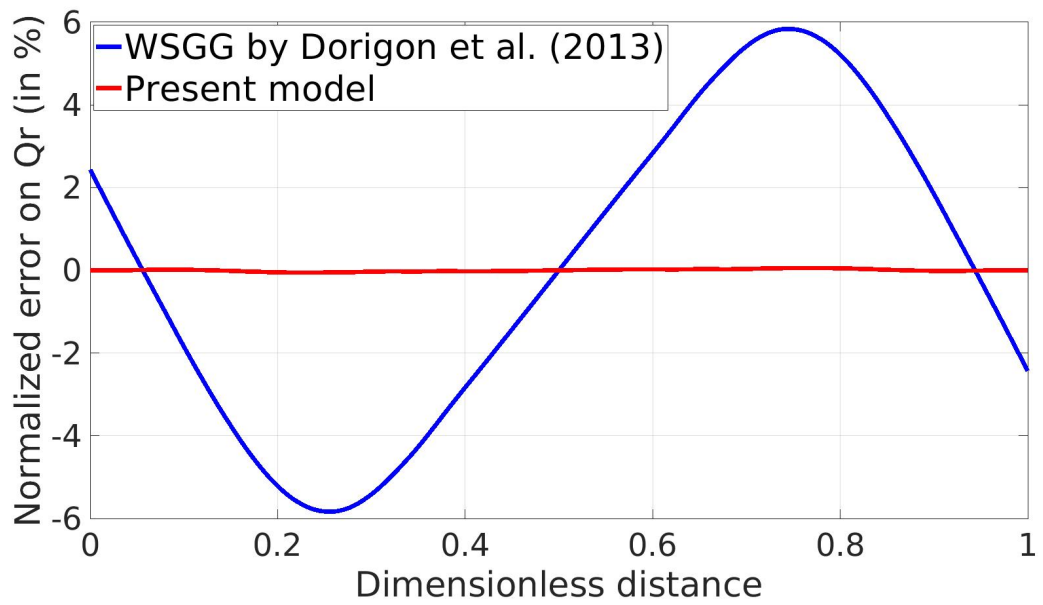
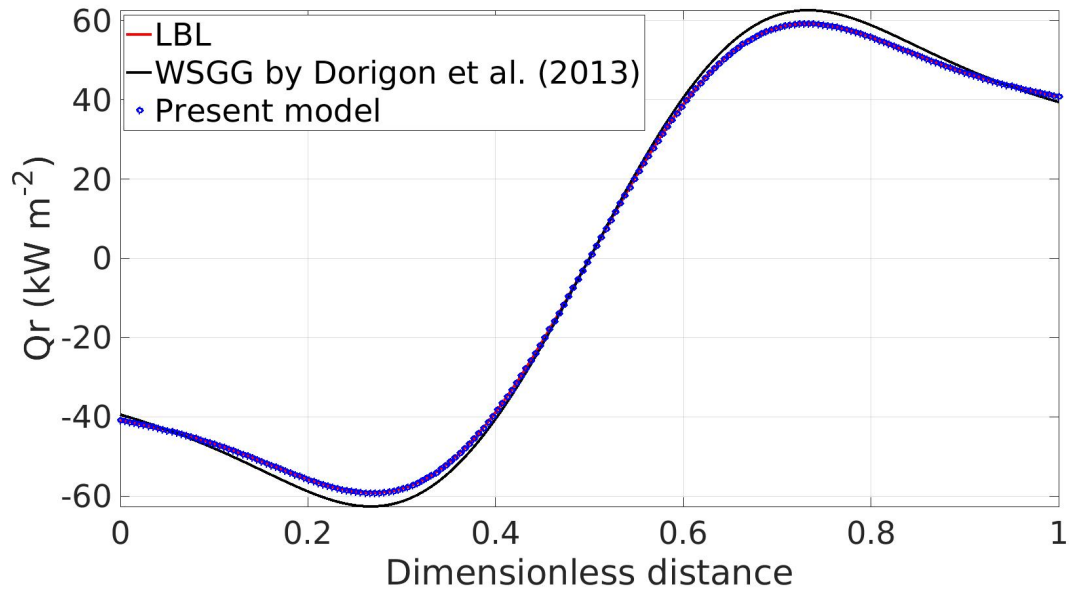
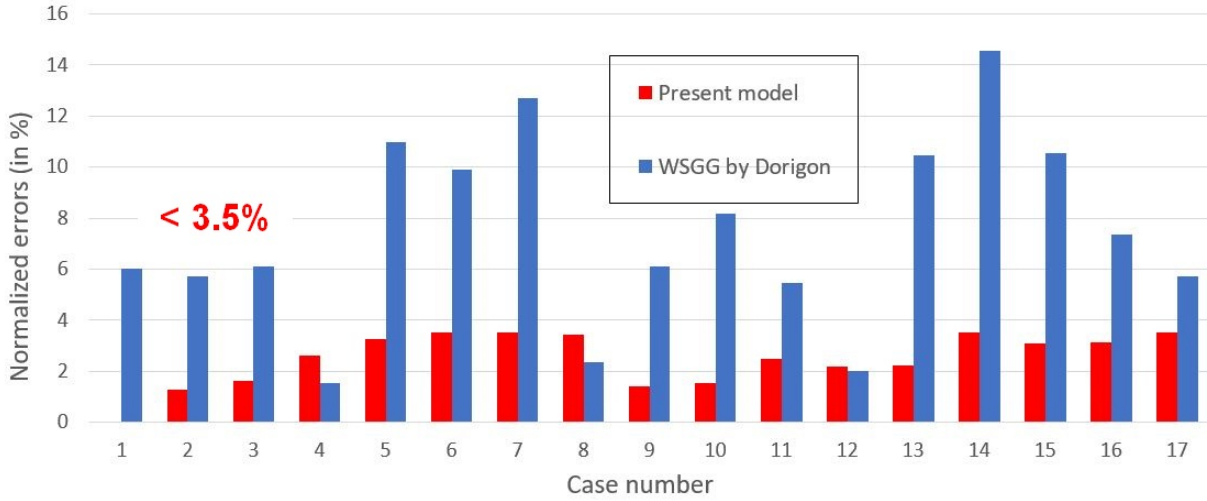
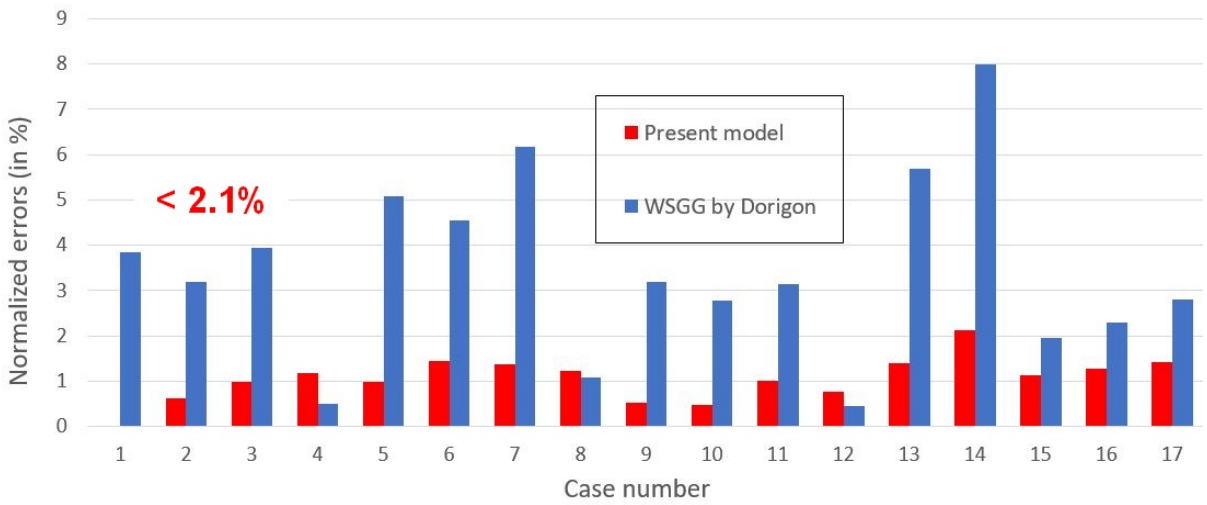


Figure 7: Comparison on Q_r obtained with the present model (for 6 gray gases), standard WSGG model and LBL method for Case 1.

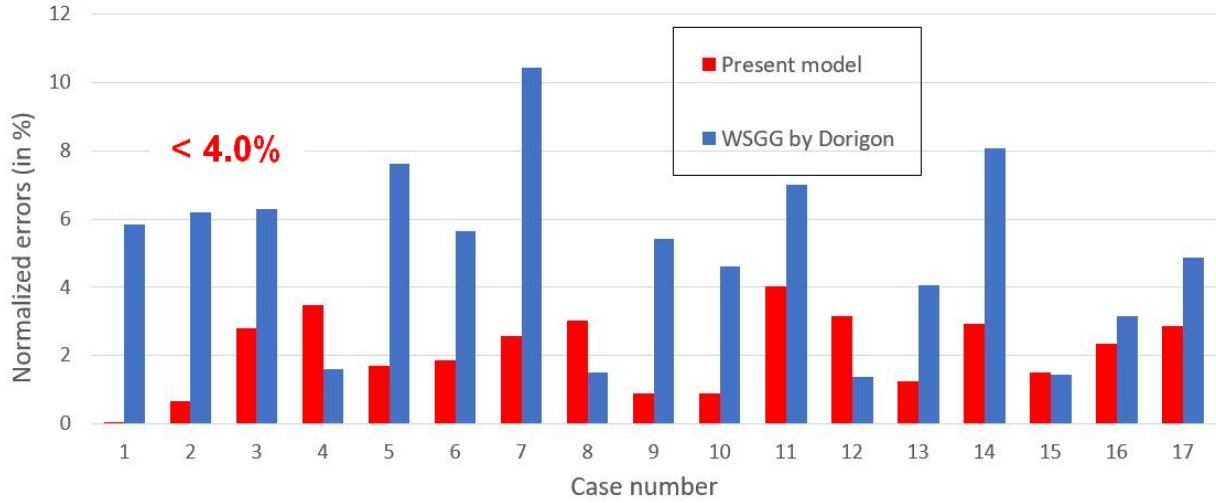


(a) δS_{\max} .

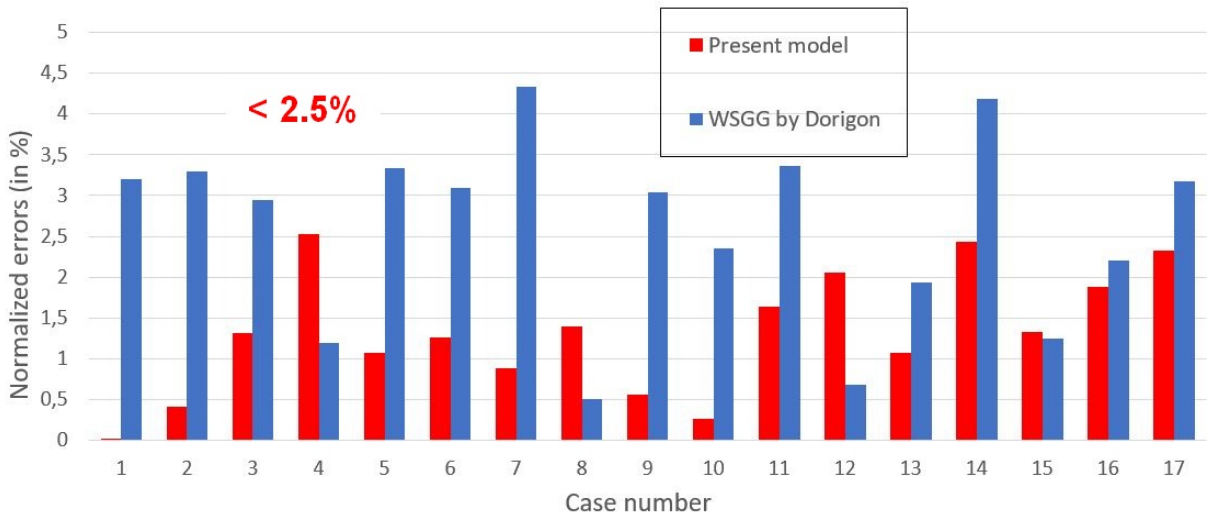


(b) δS_{avg} .

Figure 8: Maximum (δS_{\max}) and average (δS_{avg}) normalized errors on S_r obtained with the present model (for 6 gray gases) and standard WSGG model for the cases reported in Table 1, according to the LBL solution.

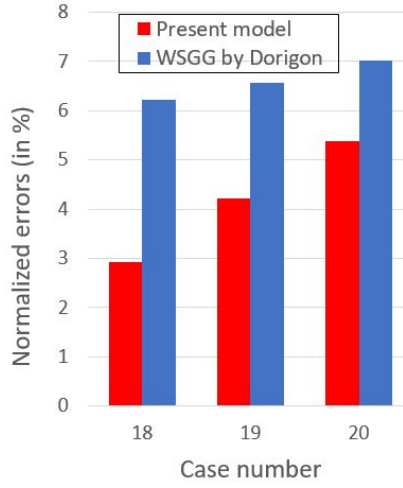


(a) δQ_{\max} .

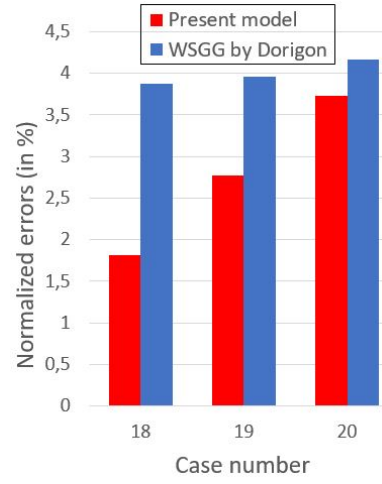


(b) δQ_{avg} .

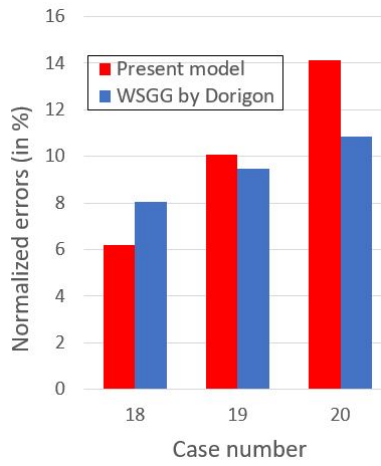
Figure 9: Maximum (δQ_{\max}) and average (δQ_{avg}) normalized errors on Q_r obtained with the present model (for 6 gray gases) and standard WSGG model for the cases reported in Table 1, according to the LBL solution.



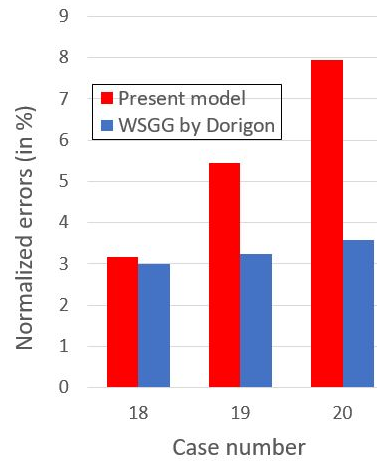
(a) δS_{\max} .



(b) δS_{avg} .

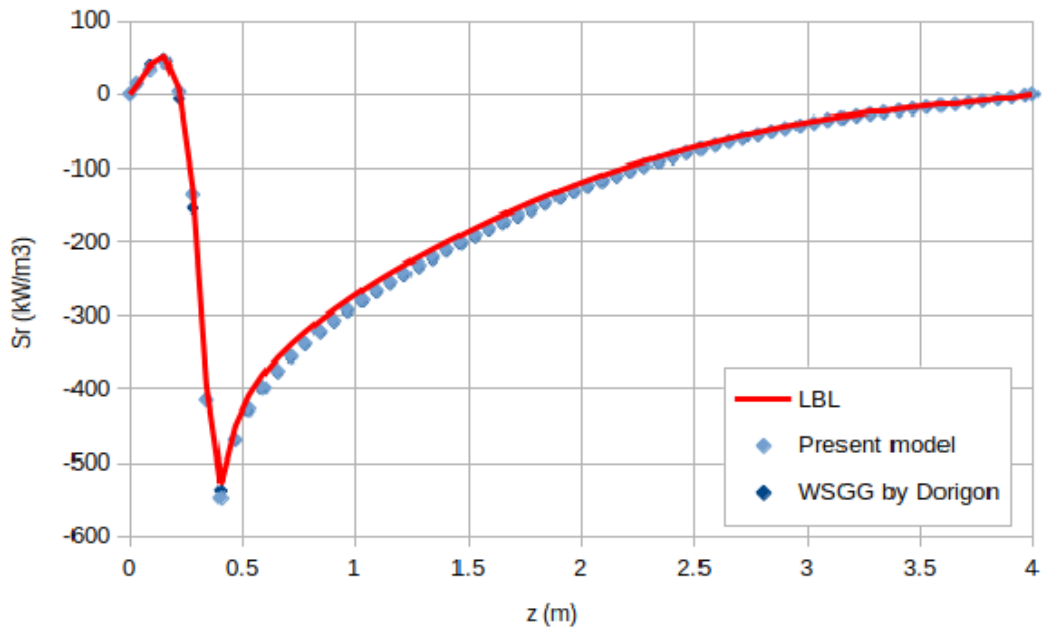


(c) δQ_{\max} .

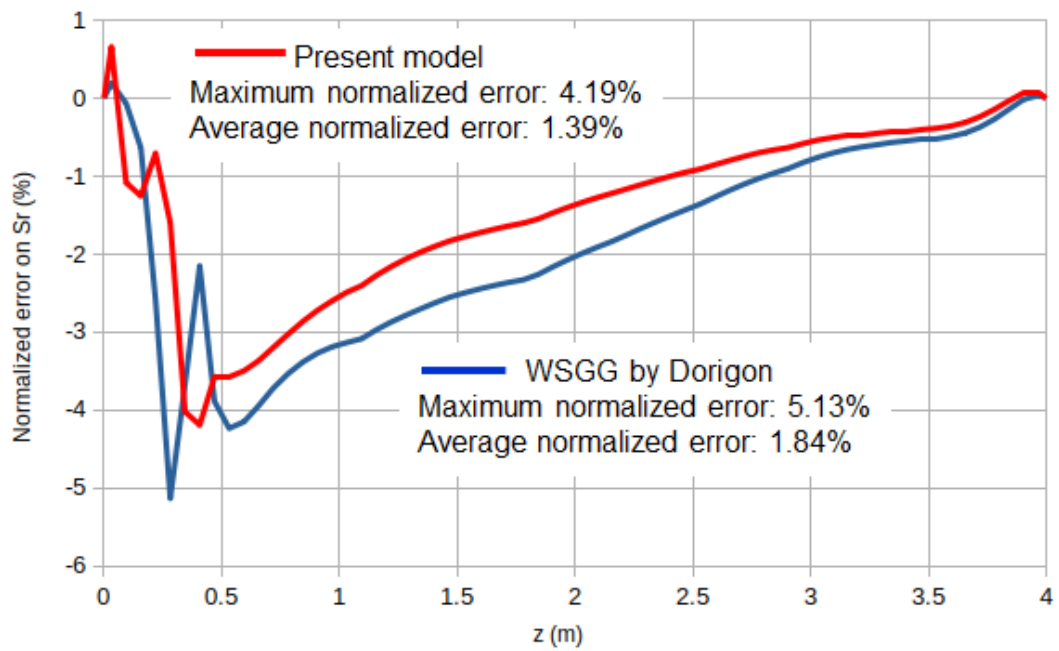


(d) δQ_{avg} .

Figure 10: Maximum ($\delta S_{\max} - \delta Q_{\max}$) and average ($\delta S_{\text{avg}} - \delta Q_{\text{avg}}$) normalized errors on S_r and Q_r obtained with the present model (for 6 gray gases) and standard WSGG model for the last three cases reported in Table 1, according to the LBL solution.

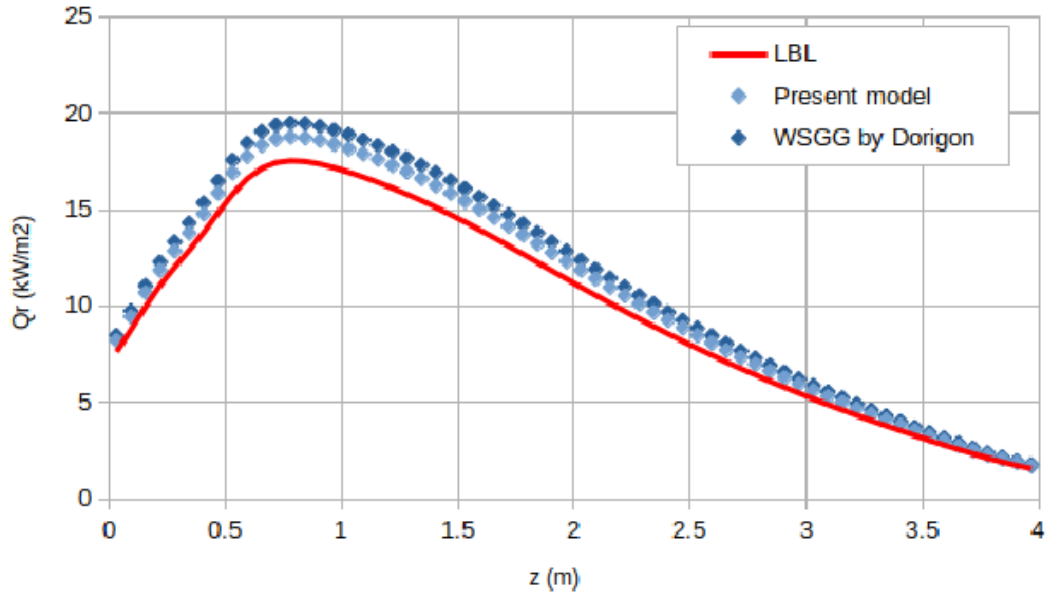


(a) Radiative heat source S_r .

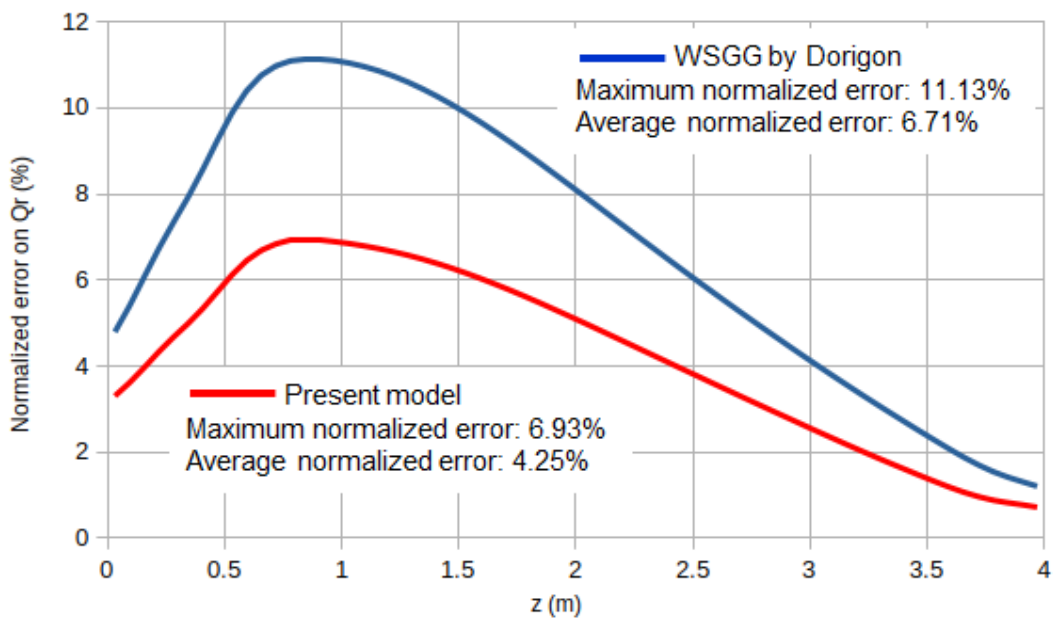


(b) Normalized error on S_r .

Figure 11: Comparison on S_r obtained with the present model (for 6 gray gases), standard WSGG model and LBL method for 3D Case with non-homogeneous gas mixture [44].



(a) Radiative heat flux Q_r .



(b) Normalized error on Q_r .

Figure 12: Comparison on Q_r obtained with the present model (for 6 gray gases), standard WSGG model and LBL method for 3D Case with non-homogeneous gas mixture [44].

List of Tables

- 1 The different cases studied. 43
- 2 Best initial guesses of parameters for the 6 gray gases model. 44
- 3 $w_1(T^{ref})$ data for the 6 gray gases model. 45
- 4 Overview of the model accuracy according to the number K 46

Case	T (K)	Y_{CO_2}	L (m)
1	Eq. (22)	0.1	1
2	Eq. (22)	0.1	0.5
3	Eq. (22)	0.1	2
4	Eq. (22)	Eq. (25)	1
5	Eq. (23)	0.1	1
6	Eq. (23)	0.1	0.5
7	Eq. (23)	0.1	2
8	Eq. (23)	Eq. (26)	1
9	Eq. (24)	0.1	1
10	Eq. (24)	0.1	0.5
11	Eq. (24)	0.1	2
12	Eq. (24)	Eq. (27)	1
13	Eq. (28)	Eq. (29)	1
14	Eq. (28)	Eq. (29)	3
15	Eq. (30)	Eq. (31)	0.25
16	Eq. (30)	Eq. (31)	1
17	Eq. (30)	Eq. (31)	2
18	Eq. (22)	0.1	3
19	Eq. (22)	0.1	4
20	Eq. (22)	0.1	5

Table 1: The different cases studied.

k	$\kappa_{p,k}^{(0)} \text{ (atm m)}^{-1}$	$w_k^{(0)}$
1	0.6382089284	0.2233136596
2	1.2344705560	0.3253242605
3	3.7243386417	0.1556371594
4	11.7017888278	0.1642889187
5	12.1322089821	0.1433675242
6	99.6564449070	0.1505063464

Table 2: Best initial guesses of parameters for the 6 gray gases model.

1-25	26-50	51-75	76-100
0.4480865666900	0.2173033559800	0.1287614383800	0.1044053640800
0.4457925217600	0.2095103134300	0.1273390805200	0.1038322176600
0.4421421719800	0.2023605799700	0.1259704001400	0.1032851313300
0.4372302625200	0.1958164576400	0.1246467926400	0.1027635710400
0.4311631243400	0.1898337476300	0.1233619668200	0.1022671709100
0.4240512193200	0.1843614242800	0.1221215916600	0.1017956529700
0.4160073562700	0.1791818386900	0.1209269764900	0.1013487837500
0.4071457311000	0.1743259976100	0.1197712817600	0.1009263424300
0.3975811107100	0.1699051771600	0.1186506190000	0.1005267264700
0.3874279789300	0.1658709652500	0.1175624041400	0.1001511881900
0.3767995689500	0.1621746564800	0.1165145424900	0.0998006535560
0.3658067411100	0.1587448567400	0.1154998783600	0.0994748150870
0.3545566882400	0.1555385905400	0.1145160822900	0.0991733855270
0.3431514821300	0.1525952872800	0.1135616932100	0.0988961020970
0.3316865469900	0.1498754293800	0.1126380453700	0.0986427263140
0.3202492824100	0.1473439096100	0.1117529479500	0.0984130430070
0.3089178240400	0.1449594470100	0.1108959178900	0.0982068593560
0.2977559541300	0.1427232261500	0.1100657684100	0.0980240040860
0.2859982863700	0.1406395837400	0.1092619234800	0.0978643267840
0.2745383241700	0.1386845895500	0.1084840676500	0.0977276973220
0.2635866148000	0.1368352733500	0.1077321000800	0.0976140053230
0.2531924938900	0.1350650157200	0.1070096908700	0.0975231596800
0.2433830282500	0.1333838694000	0.1063162144200	0.0974550881190
0.2341663877800	0.1317808064300	0.1056511632100	0.0974097368090
0.2255330851400	0.1302437722700	0.1050141573100	0.0973870700490

Table 3: $w_1(T^{\text{ref}})$ data for the 6 gray gases model.

K	Γ (in %)
1	27.9
2	7.9
3	6.2
4	4.9
5	3.7
6	3.5
7	4.0

Table 4: Overview of the model accuracy according to the number K .